Journal of Alloys and Compounds 1021 (2025) 179270

Contents lists available at ScienceDirect

Journal of Alloys and Compounds

journal homepage: www.elsevier.com/locate/jalcom

Atomic ordering and electronic structure of A_2YSn Heusler alloys: A first-principles study

Michael Zengel [a,1], Riley Nold [a,1], Thomas Roden [a], Ka Ming Law [a], Ridwan Nahar [a], Justin Lewis [a], Adam J. Hauser [a,*]

[a] Department of Physics and Astronomy, University of Alabama, Tuscaloosa, AL, United States

ARTICLE INFO

Keywords:
Heusler alloys
Density functional theory
Magnetic materials
Yttrium alloys

ABSTRACT

First-principles calculations are performed for the full Heusler $L2_1$ and inverse Heusler XA phases of the A_2YSn series, with A spanning the 3*d* block of the transition metals (A = Sc, Ti, V, Cr, Mn, Fe, Co, Ni, Cu, Zn). Yttrium is chosen as the B-site element in order to investigate the role of 4*d* B-site orbitals on the magnetic character of the system as a whole. Formation energy calculations indicate a transition from XA to $L2_1$ dominant phase preference crossing from a V to a Cr A-site element choice, with $L2_1$ remaining the dominant phase across the rest of the series. Magnetic data reveal a weak ferrimagnetic yttrium sublattice forming in a similar region of A-site valency as the phase preference transition, indicating a possible structural-magnetic coupling. Total and projected density of states calculations reveal a rich electronic structure with unique hybridization between the A-site and yttrium atoms, particularly for the $L2_1$ phase. A near half-metallic gap is found to form in the $L2_1$ phase with increasing A-site valency, culminating in a 97.71 % spin polarization for Cr_2YSn. Phase stability conclusions are also compared to data from the Open Quantum Materials Database, providing important context for the role of density functional theory (DFT) in informing material synthesis studies. These results provide new insights into the role of element choice in Heusler phase stability and electronic structure, which is critical to identifying novel materials who properties are robust against phase competition.

1. Introduction

Heusler alloys are a class of crystalline ternary intermetallics typically composed of one main group element and two transition metals, with one of the transition metals repeated twice in a unit cell. The Heusler class hosts a wide range of novel materials including half-metals [1–4,5], spin gapless semiconductors [6–8], shape memory alloys [9–11], and efficient thermoelectrics [12–14]. As a result, these alloys have found extensive application in the fields of spintronics [15,16], magnetic sensors [17], and magnetocaloric devices [18,19] among many others. The unique hybridization of these systems generates many such desirable properties not present in the separate elemental forms; for instance, the first discovered Heusler alloy (Cu_2MnAl) is ferromagnetic though none of its constituent elements possess this property [20,21]. Similarly, many Heusler systems have been shown to be highly tunable in terms of their thermal, magnetic, and transport behavior, paving the way for new advancements in tunable materials research [22–24]. Because of the variety of properties these materials possess, the identification and experimental verification of Heusler alloys useful for the development of novel technologies is an active area of research.

Half-metallicity refers to the ability of a material to preferentially conduct charge carriers of one spin orientation over the other, and alloys possessing it have clear significance in the realm of magnetoelectronics and spin electronics [25]. While this property can arise in phase pure alloys, the electronic spin gap can also be tuned via structural defects and substitutional doping [26,27]. Furthermore, ferrimagnetic coupling, or the anti-alignment of magnetic moments with different magnitudes on distinct sites, reduces the net magnetization while maintaining high spin polarization and mitigating magnetic noise in half-metals [28].

Since the 1980s, yttrium-based Heusler alloys of the form A_2YC have been known to host unique magnetic and electronic properties, including paramagnetism, superconductivity, and possible flat-band behavior, all resulting from their rich electronic structure [29–32,33].

* Corresponding author.
E-mail address: ahauser@ua.edu (A.J. Hauser).
[1] These authors contributed equally to this work.

https://doi.org/10.1016/j.jallcom.2025.179270
Received 7 November 2024; Received in revised form 15 February 2025; Accepted 17 February 2025
Available online 8 March 2025

The first discovered superconducting Heusler alloy Pd_2YSn was reported by Ishikawa et al. in 1982 [29]. Pd_2YSn's stable $L2_1$ ordering and superconducting nature were quickly confirmed by following bulk arc-melting experiments [34–36]. Au_2YIn and Cu_2YIn were also found to exhibit weak $L2_1$ ordering with intermediate degrees of antisite disorder [37–39]. Recently discovered $L2_1$-ordered paramagnets include Pd_2YMg, Ag_2YMg, Ag_2YIn, and Au_2YIn [40,41]. Alongside the A_2YC Heuslers, Y_2AC and quaternary yttrium-based Heuslers show potential for half metallicity, spintronics, and giant magnetoresistance (GMR)/tunnel magnetoresistance (TMR) [42–44]. However, bulk experimental and ab-initio studies of such materials have largely been restricted to those with a 4*d* or 5*d* block A-site element, leaving the A = 3*d* element alloys notably understudied. The few density functional theory (DFT) studies which do include certain A_2YSn alloys still report negative formation energies, but largely focus on other material systems [45]. This gap in the literature leaves unresolved questions regarding the influence of a 3*d* A-site 4*d* B-site exchange interaction on the electronic and magnetic structure of A_2YC materials. To wit, no prior comprehensive experimental or ab-initio study of the A_2YSn Heusler series (A = 3*d* transition metal) has been performed to date. Further experimental and theoretical work is recommended for comparison to the results reported here.

In this study, we report the results of first-principles density functional theory calculations performed for ten Heusler alloys of the form A_2YSn, with the A-site element spanning the 3*d* transition metals. Guided by the atomic occupation rules outlined by Burch et al. and considering the higher valency of most 3*d*-block elements compared to yttrium, we assume for this report that A-Y-Sn alloys will preferentially adopt the A_2YSn configuration rather than, for example, Y_2ASn [46,47]. Given the more delocalized nature of the 4*d* yttrium orbitals compared to the 3*d* A-site orbitals, we hypothesized the presence of unique hybridization patterns which manifested in the electronic structure and magnetic data [45]. We also sought to investigate ferrimagnetic exchange coupling between the 3*d* A-site and yttrium atoms and determine the role of said coupling in determining the magnetic behavior of the system [45,48,49]. Tin is an interesting C-site choice due to its experimental accessibility and relatively low cost. In an experimental study performed by van Engen et al. on A_2BSn Heusler alloys, those with Co and Mn as A-site elements exhibited strong signs of ferromagnetism with moments per site greater than 1 μ_B in nearly all alloys measured [50]. Given these results, we suspected the possibility of half-metallic ferromagnetism or ferrimagnetism in the series of A_2YSn (A = 3*d* transition metal), especially when the A-site is a late transition metal such as Mn to Co. Herein, we analyze the structural and electronic trends across the compositional series in terms of changing A-site valency. The results reported here may serve as a reference for future synthesis of A_2YSn alloys, providing insight into which alloys present the most interesting and thermodynamically robust electronic and magnetic properties.

1.1. The Heusler material class

Heusler alloys are ternary intermetallics with the chemical formula A_2BC, with A and B representing transition metals, and C conventionally a main group element. The Heusler structure can be viewed as four sets of interpenetrating face-centered cubic (FCC) sublattices displaced equally from each other along the [1 1 1] axis of the conventional cubic cell, with each sublattice populated by one of the four atomic species; the A species populates two of the four FCC sublattices [51]. The Heusler crystal structure is an umbrella term for two closely related cubic phases which exhibit distinct symmetries: $L2_1$ and XA, commonly referred to as the full Heusler and inverse Heusler phases, respectively [52]. These two phases differ in the atomic ordering of the two A atoms (from here on denoted A_1 and A_2) within the unit cell.

The 4-atom $L2_1$ unit cell [A_1 B A_2 C] adopts a $Fm\bar{3}m$ (No. 225) space-group symmetry, with A_1 and A_2 occupying the (0,0,0) and $(\frac{1}{2},\frac{1}{2},\frac{1}{2})$ Wyckoff sites respectively, and B and C occupying the $(\frac{1}{4},\frac{1}{4},\frac{1}{4})$ and $(\frac{3}{4},\frac{3}{4},\frac{3}{4})$ Wyckoff sites [53,54]. Typically, this structure is represented by a zinc-blende type sublattice made of the A_1 and C atoms, with the A_2 and B atoms filling the tetrahedral and octahedral holes respectively. This structure can also be viewed as a CsCl-type superstructure, with the A_1 and A_2 FCC sublattices forming a simple cubic lattice, where the B and C atoms alternatingly fill the centers of the simple cubic cells [51]. In either case, the nearest neighbor A atoms adopt an octahedral coordination.

The XA phase [A_1 A_2 B C] adopts a $F\bar{4}3m$ (No. 216) space-group symmetry, with A_1 and A_2 now occupying the (0,0,0) and $(\frac{1}{4},\frac{1}{4},\frac{1}{4})$ Wyckoff sites, and B and C occupying the $(\frac{1}{2},\frac{1}{2},\frac{1}{2})$ and $(\frac{3}{4},\frac{3}{4},\frac{3}{4})$ Wyckoff sites respectively [53,54]. As shown by Graf and Felser, the A_1 and C atoms can be thought of as forming an NaCl-type rock salt structure, with the A_2 and B atoms filling the tetrahedral holes [51]. Atomic coordination of the nearest neighbor A-atoms is more complex for the XA structure, as the A_1 and A_2 sublattices no longer coordinate to form a simple cubic setting. However, in the XA structure the A_1 and B atoms coordinate octahedrally. The relation between these two phases is that of complete antisite (swapping) disorder between the A_2 and B lattice sites. In other words, a transition from the $L2_1$ to the XA Heusler phase implies a complete "site-swap" between the A_2 and B atoms, with fixed A_1 and C sites (See Fig. 1).

1.2. Competing structural phases

Ideally, we desire a structure with as few possible phase instabilities; however, multiple disordered phases are known to exist that compete with the $L2_1$ structure. For example, site disorder between the B and C species can result in the disordered CsCl-like B2 structure ($Pm\bar{3}m$ No. 221 space group symmetry), whereas complete A-C disorder produces the BiF_3-type DO_3 structure ($Fm\bar{3}m$ No. 225 space-group symmetry) [55]. Complete disorder of the A, B, and C species across all atomic sites produces the A2 phase ($Im\bar{3}m$ No. 229 space group symmetry) [55]. A three atom C1b "half-Heusler" phase ($F\bar{4}3m$ No. 216 space-group symmetry) is also known to exist. Written with formula ABC, this phase is equivalent to an $L2_1$ structure with a A_2 site vacancy.

For this study, we will restrict ourselves to a set of element choices that has precedence for successful bulk and thin film growth, in which the A_1, A_2, and B sites are occupied by transition metals, while the C site is chosen to be a post-transition-metal main group element. Examples of such alloys include Co_2MnSi, Fe_2VAl, Co_2FeSi, Co_2TiSn, and many others [56–59,60,61]. Furthermore, given the greater chemical similarity between the A and B species (relative to say, A and C or B and C), we assume site swapping occurs more readily between these two species than for other conceivable combinations of atomic disorder [62–65]. Therefore, we restrict our attention to only competition between the $L2_1$ and XA phases, treating local antisite-swap disorder between the A_2 and B site as the dominant defect mechanism.

The competition between the $L2_1$ and XA structures, and thus by extension the degree of A-B antisite disorder, can be roughly quantified by the difference in formation energies between the respective phases. This convention for approximate $L2_1$-XA phase preference has been used by Ma et al, Luo et al, and others with great success [66–68]. A high formation energy difference implies that one cubic phase is more likely to form over the other. In practice, this means that the risk of unintended antisite disorder of a sample is reduced. It is therefore critical to identify material candidates with either thermodynamically protected properties (strong phase preference) or whose principal features vary little with inevitable site-swap disorder.

We also note that alongside the inherent thermodynamic competition between the identified cubic phases, the manufacturing of these alloys in a bulk or thin film setting may result in multiphase samples. This phase competition could be varying or discrete intermediate degrees of disorder, or competing combinations of ternary, binary, or

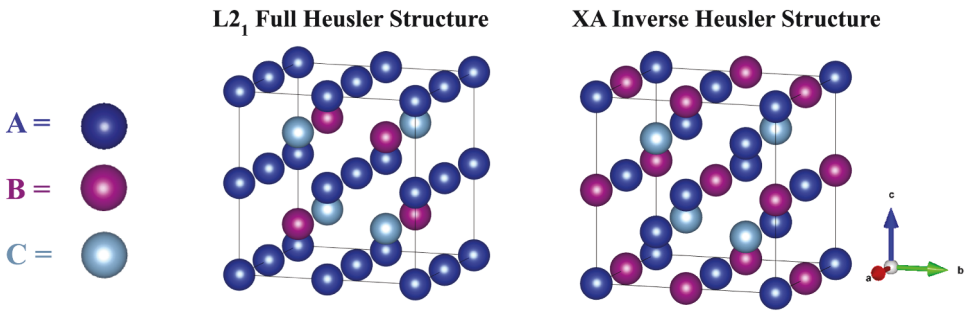

Fig. 1. Crystal structure of $L2_1$ and XA Heusler phases exhibiting antisite disorder relation. For consistency, the stationary A_1 atom is set at the (0,0,0) site in both structures.

single-element phases [69–72,73]. When considering ternary and quaternary Heusler systems, the resultant phases depend strongly on the manufacturing and post-annealing temperatures utilized [74,75]. For example, Hirohata et al. finds that the 2d layer-by-layer growth process typical in thin film production can significantly reduce the crystallization energy of certain Heusler materials compared to bulk, allowing for the stabilization of samples with higher phase purity [76]. In short, experimental processes and energetic phase competition play important roles in the realization of phase-stable Heusler alloys. While confounding experimental factors cannot and will not be the focus of our density functional theory analysis, computational results may be of value to guide potential bulk and thin film studies of A_2YSn type Heuslers.

1.3. Effect of disorder on electronic structure

In order to gain a holistic understanding of antisite disorder, we must first provide a brief description of the electronic structure of the pure $L2_1$ (and XA) phases. In both phases, the core *s* and *p* orbitals are tightly bound and buried well below the Fermi level. On the other hand, electronic states with strong *d*-character are relatively closer to the Fermi energy ($\sim \pm$ 10 eV) and thus strongly dictate the functional electronic properties of the system. Furthermore, the tightly packed structure of a Heusler alloy causes the *d*-orbitals on the atoms to overlap significantly; in other words, this close-knit arrangement forces a considerable degree of *d*-orbital hybridization, which highly depends on the occupancies of these *d*-orbitals [53]. In the case of a general Heusler alloy comprised of a *p*-block C-site atom and transition metal A- and B-site atoms, the differences in electronegativities and electron orbital shapes of adjacent atoms lead to varying degrees of hybridization [54,77]. For example, the Fe *s* and *p* orbitals in Fe_2VAl, hybridize with the Al *s* and *p* orbitals within a zinc-blende sublattice. The *d*-orbitals from Fe are thus free to hybridize with the other Fe atom, given their near-identical environment, and the *d*-orbitals on V form the upper and lower band edges in the minority band of Fe_2VAl [53]. In other words, the low energy hybridization between the *p* block element and one of the A-site transition metals generates a sublattice from which the other orbital arrangements can be understood. Site disorders, especially antisite disorders which represent mixed occupation of A-site and B-site, tend to narrow the minority band gap, reducing the spin polarization and the magnetic moment per site [53].

2. Methodology

First principles calculations are performed on ten Heusler alloys of the form A_2YSn, where the A-site is occupied by a 3*d*-transition metal. Differences in cohesive energy between the two identified Heusler phases ($L2_1$ and XA) are tabulated for each alloy in order to quantify the robustness of key material properties (half-metallicity, magnetic ordering, etc.) against antisite-swap disorder. Trends in the magnetic and electronic structure dependent on the A-site valency are examined for prospective property-tuning applications via substitutional doping.

All raw computational data (excluding electronic band calculations) has been published in Data in Brief Volume 52 as part of an overarching high-throughput DFT project [78]. Calculated band structures can be found in Appendix A.

2.1. Computational Procedure

First principles calculations were performed via the projector augmented wave (PAW) method in the Quantum Espresso 6.8 package [79,80]. The generalized gradient approximation (GGA) is applied to the exchange-correlation energy functional, and the atomic scalar-relativistic Perdew-Burke-Ernzerhof (PBE) pseudopotentials developed by Dal Corso were used [81,82]. The DFT+U method is not implemented for these calculations to preclude potential unphysical broadening of half-metallic gaps [83]. Additionally, manually tuning a U parameter in order to reproduce well-known lattice parameters and magnetic moments is unfeasible given the scarcity of experimental studies characterizing A_2YSn Heusler alloys.

The wavefunction and charge-density cutoff energies were not explicitly optimized for each alloy, but instead fixed at 250 Ry and 1000 Ry respectively. These values were found to be sufficiently high to minimize any meaningful error in cohesive energies calculated. A 4-atom Wigner-Seitz unit cell is used for each alloy, with atomic positions dictated by either the $L2_1$ or XA ordering. Structural optimization was achieved via iterated self-consistent field (SCF) calculations followed by a variable-cell relaxation (vc-relax) calculation utilizing the Broyden-Fletcher-Goldfarb-Shanno (BFGS) minimization technique. Starting atomic moments were set to 0.01 μ_B for non-magnetic atoms and 1.00 μ_B for strongly magnetic atoms (Fe, Co, Ni), which then vary in sign and magnitude during the self-consistent cycle until a minimum energy state is achieved. For our purposes, only collinear magnetic configurations are considered. Spin-orbit coupling (SOC) contributions were found to have negligible effect on the electronic density of states for the largest A-site element alloy in the series (Sc_2YSn). SOC effects are therefore neglected for the rest of the report, although such contributions may provide an avenue for further research into the A_2YSn series.

For the initial SCF calculations a $10 \times 10 \times 10$ Monkhorst-Pack k-point grid and a 10^{-6} Ry energy convergence threshold were used. For Brillouin zone integration, occupations were handled with a standard Gaussian smearing method with a degauss (broadening) parameter of 0.002. The total cohesive energy of the alloy was calculated for a variety of lattice constants in order to produce a cohesive energy vs. unit-cell volume plot. The "best-fit" SCF lattice parameter, bulk modulus, and bulk modulus pressure derivative were determined by fitting these data against the standard Birch-Murnaghan equation of state [84]. The best-fit SCF lattice parameter was used to determine the input cell-volume for the vc-relax calculation, which allows minor variations in the lattice parameters as well as the atomic positions around the strict FCC coordinates. Due to the nature of the vc-relax calculation and initial cubic symmetry of the corresponding stress tensor, the initial cubic symmetry of the Heusler alloy is maintained throughout the relaxation

process. In other words, a purely cubic phase is assumed throughout the computational process. With a primary focus on cubic $L2_1$-XA phase disorder, stability of the A_2YSn series against tetragonal distortion is not considered in this study. However, given the role tetragonal distortion plays in stabilizing some XA-like Heusler phases, such calculations may prove a fruitful avenue for later investigations [85]. All vc-relax calculations were performed with a $20 \times 20 \times 20$ k-point grid and 10^{-9} Ry energy convergence threshold. The lattice parameters and structure resulting from the vc-relax step were taken as the final optimized structure of the calculation sequence and is assumed for following electronic and energetics calculations.

A final SCF calculation was performed to determine the precise cohesive energy and site-specific atomic moments of the optimized structure. A $20 \times 20 \times 20$ k-point grid with 10^{-9} Ry energy convergence threshold was used for increased precision. The gaussian smearing was replaced by a tetrahedral interpolation method better suited for both precise energetics and the electronic structure calculations which followed [86,87].

A non-self-consistent field (NSCF) approach was taken to produce the density of states (DOS) and electronic band structure data. DOS and band calculations were performed in an adjustable alloy-specific energy range that was modified to produce data within a range of at least $\pm$ 4 eV of the Fermi energy. Spin polarization at the Fermi energy (S) is calculated as an absolute percentage via the following formula:

$$S = \left|\frac{N_\uparrow - N_\downarrow}{N_\uparrow + N_\downarrow}\right| \times 100\%$$

Where $N_\uparrow$ and $N_\downarrow$ are the majority and minority DOS measured at the Fermi energy.

For band calculations, the energy resolution was fixed at 0.001 eV. A conventional k-path $[\Gamma{-}X{-}W{-}K{-}\Gamma{-}L{-}U{-}W{-}L{-}K]$ connecting various high-symmetry points of the Brillouin-Zone is used (see Fig. 2). The electronic structure of the A_2YSn series will be discussed primarily in regard to the density of states. Further details regarding the calculated band structure diagrams can again be found in Appendix A. Crystal structure diagrams were generated in the Vesta visualization software [88].

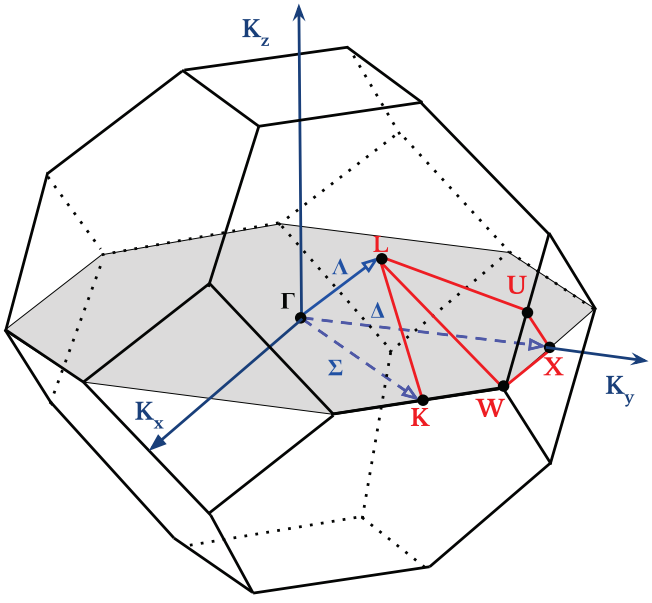

Fig. 2. Brillouin zone of FCC crystal with relevant high-symmetry points depicted.

3. Results and discussion

3.1. Structural properties

Optimization of each A_2YSn structure was achieved via a combination of increasingly resolved SCF and vc-relax calculations, as detailed above. Total cohesive energy is plotted against the unit-cell volume and fitted according to the Birch Murnaghan equation of state. Best-fit lattice parameter, bulk modulus (GPa), and bulk modulus pressure derivative values for the strict FCC unit cell were determined for each phase. Fig. 3 shows a representative cohesive energy plot for the Mn_2YSn system, which preferentially adopts the full Heusler $L2_1$ structure.

The cohesive energy difference for the $L2_1$ and XA phases (ΔE) is reported for each material. For each material, ΔE is calculated as the difference in cohesive energies for the $L2_1$ (E_{FH}) and XA (E_{IH}) phases. A positive ΔE is taken to mean the XA phase is more energetically favorable ($E_{IH}<E_{FH}$) and hence is the "preferred" structure, whereas a negative ΔE implies $L2_1$ is the energetically favorable phase ($E_{IH}>E_{FH}$). Predicted physical properties are reported for all materials in table 1. As previously mentioned, to the authors knowledge no experimental structural, elastic, or magnetic data have been reported to date for the A_2YSn (A = 3*d* transition metal) series. Further experimental work is recommended to contextualize the results given here.

Both the $L2_1$ and XA optimized lattice parameters show a clear dependence on the choice of A-site element, as shown in Fig. 4. The optimized $L2_1$ lattice constant decreases with increasing A-site valency until a minimum value of 6.44112 Å for A = Co, after which the lattice parameter increases again. The optimized XA lattice parameters follow a similar trend, where the minimum value is reached at A = Ni. For both phases lattice constant anomalies are observed from A = V to A = Mn, where the optimized lattice parameters do not follow the larger concaving trend. For instance, the lattice parameter of Cr_2YSn-XA is not smaller, but larger, than that of V_2YSn-XA by an exceptional amount of 0.20 Å. Furthermore, this brief upturn coincides with a change of sign in ΔE, i.e., a change of phase preference from XA to $L2_1$.

The magnitude of ΔE indicates the robustness of these phases against A-B antisite defects. As seen in Fig. 4, for A-site choices with a valency of five or less (A = Sc, Ti, V), the XA structure is slightly preferred over $L2_1$, with a ΔE in the range of 0.01–0.06 eV/atom. At A = Cr (valency = 6), there is a large drop in ΔE to −0.395 eV/atom, implying a strong reversal in phase preference from XA to $L2_1$. From A = Cr onward, $L2_1$ remains the energetically dominant phase for the A_2YSn alloys, with ΔE staying below at least −0.07 eV/atom. We note an immediate spike in ΔE near A = Mn and A = Fe, relative to the −0.395 eV/atom observed

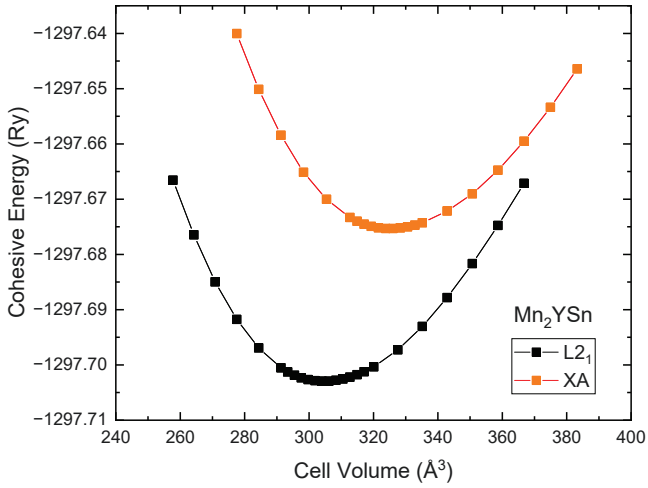

Fig. 3. Mn_2YSn cohesive energy per unit cell (Ry) plotted against unit cell volume (Å^3) for the full Heusler $L2_1$ and inverse Heusler XA phases.

Table 1
Final SCF Computational Results: Lattice constant (a), bulk modulus (B), bulk modulus pressure derivative (B_p), cohesive energy difference (ΔE), magnetic moments, spin-up and spin-down electronic band gaps ($E_g\uparrow$ and $E_g\downarrow$), and spin polarization at the Fermi energy (S) for both $L2_1$ and XA phases of A_2YSn Heusler alloys (A = Sc, Ti, V, Cr, Mn, Fe, Co, Ni, Cu, and Zn). Bulk modulus pressure derivative (B_p) calculations were also attempted for Zn_2YSn but did not produce estimates within a reasonable numerical range, and are therefore not reported. For spin-resolved data the positive z-direction (with respect to the 4-atom unit cell) is chosen as the spin-up direction.

Alloy	Phase	a (Å)	B (GPa)	B_p	ΔE (eV/atom)	Site Moments (μ_B)				Total Moment (μ_B/f.u)	$E_g\uparrow$ (eV)	$E_g\downarrow$ (eV)	S (%)
						A_1	A_2	B	C				
Sc_2YSn	$L2_1$	7.30447	152.2	4.11	0.021438	0.3528	0.3528	0.3641	−0.0178	1.64	0.000	0.123	17.17 %
Sc_2YSn	XA	7.34166	151.3	7.62	-	0.2073	0.2944	0.1018	−0.0110	0.88	0.000	0.000	21.90 %
Ti_2YSn	$L2_1$	6.91611	214.7	4.26	0.056071	0.2016	0.1998	0.1945	−0.0137	0.83	0.000	0.000	56.20 %
Ti_2YSn	XA	7.01941	205.8	4.12	-	0.6672	1.3681	0.0946	−0.0474	2.67	0.015	0.023	65.49 %
V_2YSn	$L2_1$	6.89383	193.8	2.11	0.009110	2.4894	2.4894	0.3728	−0.0758	6.36	0.492	0.000	20.52 %
V_2YSn	XA	6.75643	260.5	3.56	-	0.0002	0.0000	0.0000	0.0000	0.00	0.115	0.115	0.03 %
Cr_2YSn	$L2_1$	6.67589	265.7	3.09	−0.395258	2.3543	2.3539	0.0641	−0.0912	4.99	0.109	0.000	97.71 %
Cr_2YSn	XA	7.02784	149.5	3.85	-	3.2708	0.8249	−0.0148	−0.0701	4.21	0.360	0.000	32.83 %
Mn_2YSn	$L2_1$	6.73158	166.8	3.70	−0.094349	3.3179	3.3179	−0.1677	−0.0697	6.33	0.000	0.268	34.62 %
Mn_2YSn	XA	6.88101	163.3	4.13	-	3.6372	3.7559	−0.0867	−0.0441	7.36	0.000	0.000	50.19 %
Fe_2YSn	$L2_1$	6.57387	241.1	5.26	−0.076897	2.4445	2.4446	−0.2054	−0.0271	4.39	0.000	0.224	66.42 %
Fe_2YSn	XA	6.68259	229.1	4.39	-	2.6832	2.6666	−0.0624	−0.0090	5.13	0.049	0.057	31.47 %
Co_2YSn	$L2_1$	6.44112	295.2	4.29	−0.374110	0.6793	0.6793	−0.0880	−0.0158	1.05	0.000	0.095	58.34 %
Co_2YSn	XA	6.63011	228.9	4.61	-	1.5675	1.8193	−0.0419	0.0333	3.27	0.000	0.050	89.76 %
Ni_2YSn	$L2_1$	6.49927	257.7	4.76	−0.310577	−0.0142	−0.0032	0.0008	−0.0005	−0.02	0.000	0.000	8.13 %
Ni_2YSn	XA	6.59917	220.8	4.72	-	0.0000	0.0001	0.0000	0.0000	0.00	0.080	0.081	0.07 %
Cu_2YSn	$L2_1$	6.65229	190.3	18.87	−0.207711	0.0000	0.0000	0.0000	0.0000	0.00	0.000	0.000	0.00 %
Cu_2YSn	XA	6.75839	187.5	4.00	-	0.0000	0.0000	0.0000	0.0000	0.00	0.000	0.000	0.00 %
Zn_2YSn	$L2_1$	6.98731	141.5	-	−0.071413	0.0000	0.0000	0.0000	0.0000	0.00	0.000	0.000	0.00 %
Zn_2YSn	XA	7.05710	127.1	-	-	0.0000	0.0001	0.0002	0.0000	0.00	0.000	0.000	0.64 %

for a Cr A-site, after which ΔE quickly drops down again to around −0.374 eV/atom. From A = Co on, ΔE increases monotonically implying a weakening of the $L2_1$ phase preference and the possibility of increasing antisite-swap disorder. The phase preference transition can be understood both from the magnetic moments data and general experimental rules for Heusler-type materials. Firstly, the onset of higher A-site magnetic moments is observed in both phases starting around A = V and continuing through A = Co. In the $L2_1$ structure, the two A-site elements are no longer nearest neighbors, making this phase more preferential for A-sites with high magnetic moments via a reduction of the associated A_1-A_2 spin-spin exchange energy. Similarly, widely accepted experimental rules established by Burch et al. [46,47] predict the transition metal with the higher valency tends to preferentially occupy the (0,0,0) and $(\frac{1}{2},\frac{1}{2},\frac{1}{2})$ atomic sites. Therefore, despite the reduction in A-site magnetic moments observed for A = Ni through A = Zn, the high A-site valency still results in an overall $L2_1$ phase preference. For the low A-site valency alloys (A = Sc, Ti, V), the relatively low A-site moments along with a weak Burch-rule preference allow for the XA phase to remain stable against the $L2_1$ ordering.

3.2. Magnetic properties

The structural ordering trends seen in the previous subsection match closely the behavior of the magnetic moments observed for the A_2YSn series. Total moments for each material and phase are show in Fig. 5(c) as a function of the A-site. The primary contribution to the total magnetic moment comes from the two A element atoms, with only small contributions from the Sn site. For the $L2_1$ structures the total moment is found to peak at both A = V and A = Mn, with values of 6.36 and 6.33 μ_B respectively, after which the total magnetic moment falls off to zero with increasing A-site valency. The XA structures likewise have a peak in total moment at A = Mn of 7.36 μ_B. Here, the unexpected decrease in total moment for the $L2_1$ phase between A = V and A = Mn can be explained by changes in the magnetic moments of the yttrium sublattice in response to the increasing A-site valency.

Site-specific magnetic moments calculated for each material and structural phase are shown in Fig. 5(a,b) plotted against the A-site element. While the A_1 and A_2 sites in $L2_1$ are essentially equivalent, we compared these two site moments to ensure that the vc-relaxation step did not cause sufficient change to make the sites functionally unequal. Any differences generated for the $L2_1$ phase were not significant and contrast strongly the large site differences of the inequivalent A_1 and A_2 sites in the XA phase. Besides a small dip in moment at A = Cr, both the A_1 and A_2 atoms of the $L2_1$ structures exhibit increasing site moments with an increasing A-site valency, until a maximum moment of 3.32 μ_B is achieved at A = Mn. As we cross the phase preference transition threshold the yttrium atom moment becomes significantly reduced in magnitude, dropping from 0.37 to 0.06 μ_B, and eventually flipping to become antiparallel with respect to the A_1 and A_2 moments. The antiparallel yttrium moment maxes out at A = Fe with a moment of −0.205 μ_B. The onset of an increasingly ferrimagnetic yttrium site character explains the drop in the total moment observed after crossing the phase preference threshold, as the yttrium moment no longer positively contributes to total moment. Likewise, the C-site Sn atoms align antiparallel to the A-site moments, albeit with a much smaller moment as to make the effect on the total moment unnoticed. The Sn moments peak in magnitude with A = Cr at around −0.09 μ_B.

As for the XA structures, peaks in the A_1 and A_2 moments are also seen at A = Cr, similar to the $L2_1$ structures. However, trends in the A_1 and A_2 moments are no longer identical due to differing atomic environments for the two A-element sublattices in the XA ordered phase. Deviations between these two moments may arise from distinct coordination of A_1 and A_2 sublattices with the yttrium sublattice, giving rise to differing degrees of exchange interaction. Nevertheless, the yttrium atoms of the XA structures also exhibit a ferrimagnetic character with regards to the A_1 and A_2 moments, although with a reduced site moment relative to the moments calculated for the $L2_1$ phase. Here, the antiparallel yttrium moment peaks at A = Mn with a moment of −0.087 μ_B. The Sn atoms also generally align antiparallel to the A-element moments, except for A = Co where Sn adopts a small positive moment of around 0.03 μ_B.

The influence of the A-site valency on the magnetic behavior of the system can be understood as arising from two distinct effects. Firstly, different A-site choices will contribute a different moment to the system depending on the magnetic character of the element in question, resulting in variations of the A-site and total magnetic moment. In addition, it is well known that the strength and character (ferromagnetic vs. antiferromagnetic) of the magnetic exchange coupling in the Heusler system is strongly dependent on the interatomic distance between the

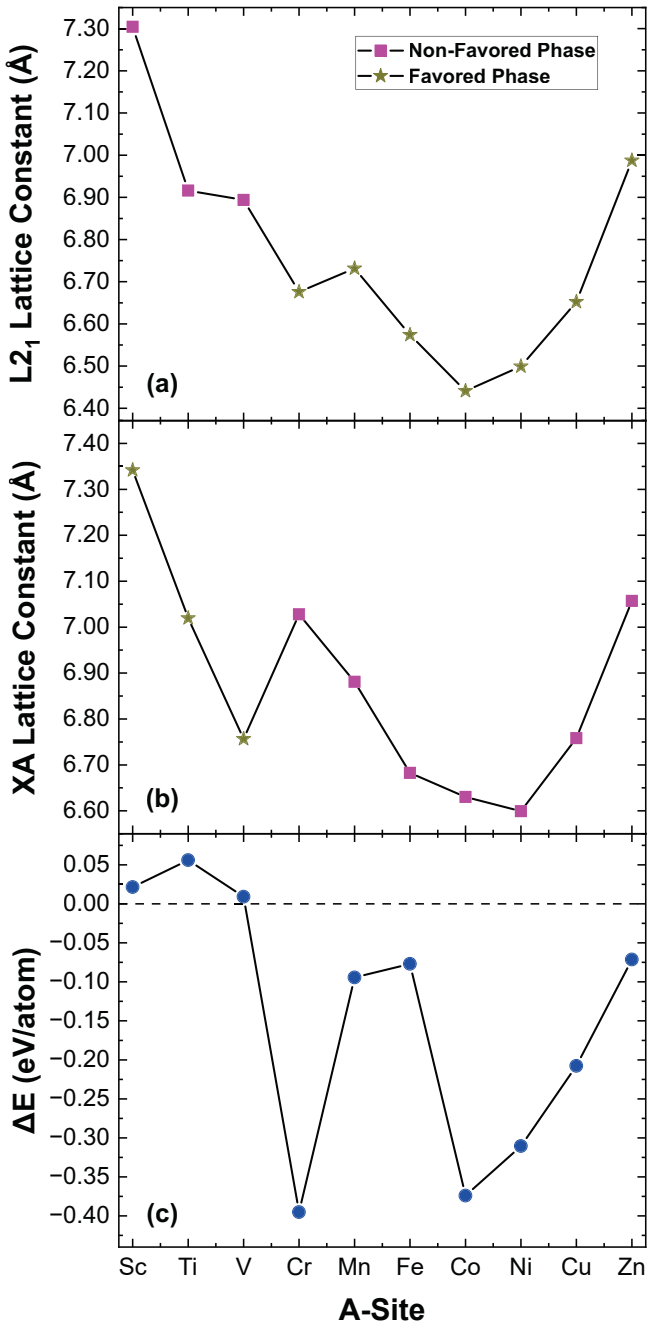

Fig. 4. Dependence of a) $L2_1$ and b) XA optimized lattice constants with respect to varying A-site. The favored phase for each A-site is denoted by a gold star, while the non-favored phase is represented by a pink square. c) Difference in $L2_1$ and XA cohesive energies (ΔE) for varying A-site elements. A transition from XA dominant ordering to $L2_1$ dominant ordering is observed moving from A = V to A = Cr. The $L2_1$ phase preference is maintained for all alloys with an A-site valency of six or greater.

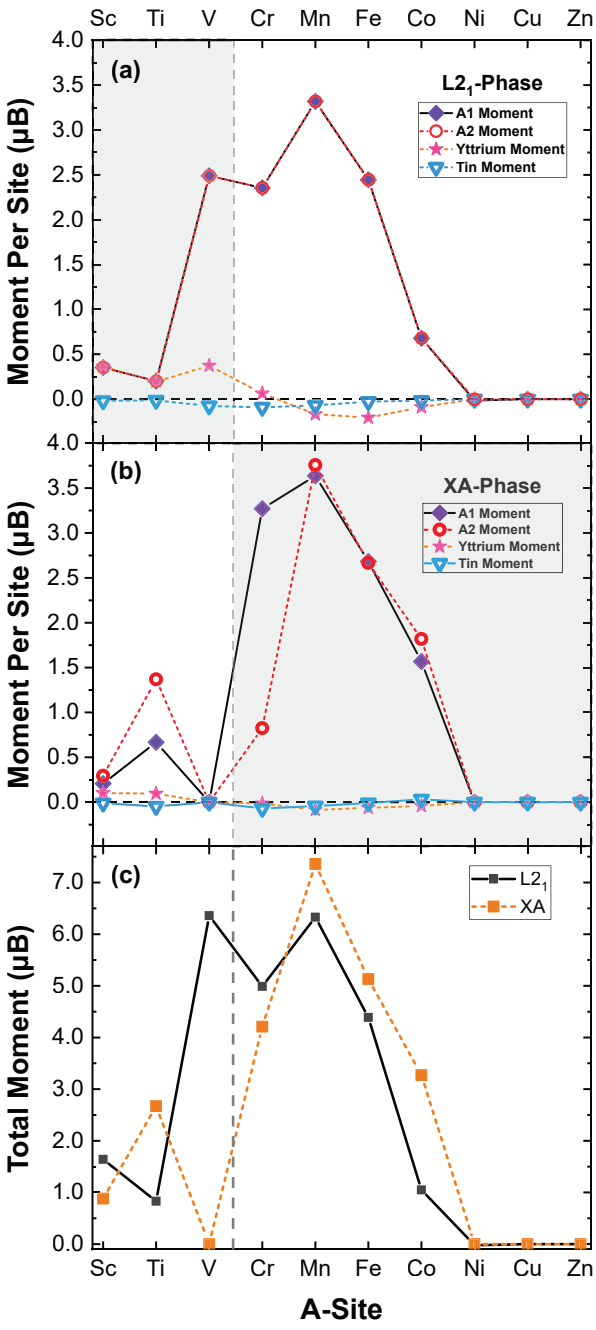

Fig. 5. Site specific magnetic moments versus A-site element for both the a) $L2_1$ and b) XA structural phases. Non-shaded regions indicate favored phases. Horizontal dashed lines mark the value of a 0 μ_B site moment. c) A_2YSn total magnetic moment (μ_B) versus A-site element for both the $L2_1$ and XA phases. Peaks in the total moment of around six to seven μ_B are observed at A = Mn for both structures. A vertical dashed line is included across all plots to demarcate the transition from XA to $L2_1$ ordering preference.

coupled atoms (typically the A1-A2 or A-B sites)[18,89]. As a result, variations in the dominant phase lattice constant with changing A-site valency (see Fig. 4) play an important role in the magnetic character of the A_2YSn system. For example, the three $L2_1$-dominant alloys with the highest total moment (A = Cr, Mn, Fe) show a variation in A-site moment and total moment (Fig. 5) which is similar to the variation in the $L2_1$ lattice constants for these three alloys. In short, both the intrinsic moment of the A-site element and induced variations in the dominant phase lattice constant modulate the magnetic behavior of the A_2YSn system.

Likewise, calculations for both structural phases reveal a ferrimagnetic yttrium sublattice which forms with increasing A-site valency, further explaining the anomalies observed in the total moments of these materials. The onset of this ferrimagnetic behavior in conjunction with the XA-$L2_1$ phase preference transition indicates a possible structural-magnetic coupling, such that the magnetic character of the yttrium sublattice may be tuned through careful control of the alloys phase near the phase-preference transition region. Such tunable ferrimagnetic materials have been shown to offer new magnetic degrees of freedom in designing spintronic devices [90–92]. However, rigorous confirmation

of any structural-magnetic coupling would require further theoretical and experimental verification.

3.3. Electronic structure

3.3.1. Spin polarization

A general trend is observed between spin polarization and the atomic radius (van der Waals radius) of the A-site element, as seen in Fig. 6[93]. Note that the ordering of A-site elements by increasing atomic radius does not strictly follow the same order as that of valence electron count (i.e., order on the periodic table). For the $L2_1$ structures the absolute spin polarization increases steadily with increasing A-site atomic radius until a maximum of 97.71 % is achieved at Cr_2YSn-$L2_1$ with a A-site atomic radius of 1.89 Å, after which the spin polarization decreases monotonically (with the exception of the jump between Fe and Co). For the XA structures, a similar increase in spin polarization is observed in the region of 1.8–2.0 Å, with a maximum of 89.76 % for Co_2YSn-XA at 1.92 Å. However, the XA structures show a much more abrupt jump in spin polarization around the 1.8–1.85 Å region, with sharp oscillations in spin polarization rather than smooth behavior.

Dependence of the absolute spin polarization on the A-site van der Waals atomic radius may be explained by variations in the A-B *d*-orbital overlap which typically contributes to the half-metallic behavior [94]. The increased atomic radii of the A_1 and A_2 sites will improve orbital overlap with the B-site element and hence the *d-d* hybridization of the transition metals, modifying the A-B site exchange interaction and contributing to the half-metallic character. However, for a fixed crystal structure the increasing A-site atomic radius results in a generally larger unit cell, decreasing the degree of *d-d* orbital overlap. The balance of these two effects seems to give rise to a region of optimal A-site atomic radii where half-metallic effects may be observed, resulting in peaks in the spin polarization. Spin polarization trends are discussed further in 3.3.2 in context of the DOS and PDOS data.

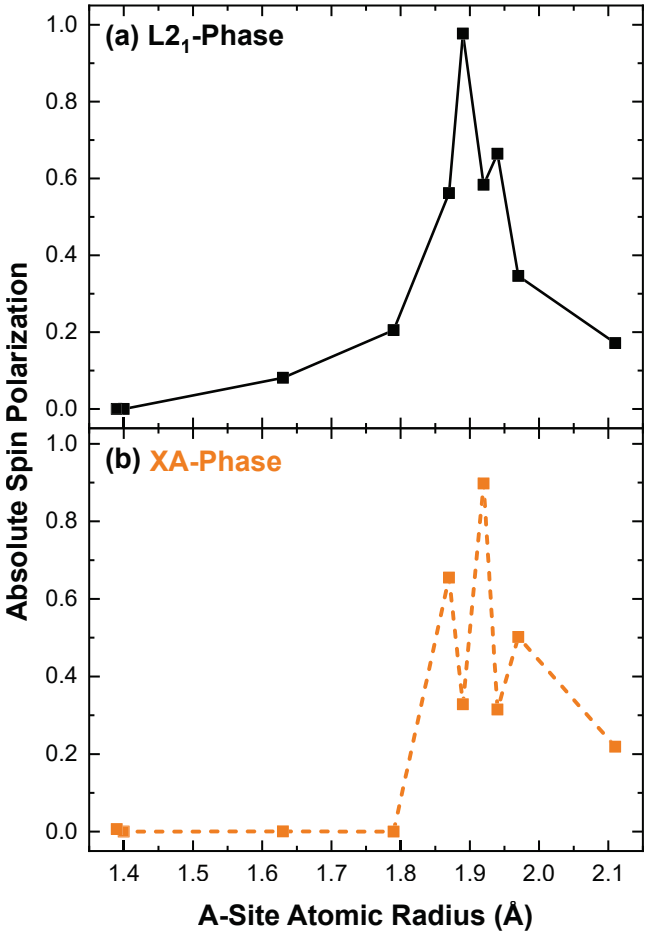

Fig. 6. Absolute Spin Polarization plotted against the A-site van der Waals atomic radius (Å) for the $L2_1$ and XA phases. Peaks in the absolute spin polarization are seen in the range of 1.8–2.0 Å.

Based upon the foundational work of Slater and Pauling in the 1930's, as well as modern density functional theory investigations, it has been well-documented that the total magnetic moments of 3*d* Heusler alloys which exhibit half-metallic ferromagnetism can be predicted via the total valence electron counts of their constituent elements [82,95,96]. However in this series the only strong half-metallic ferromagnet (spin polarization above 90 %) is the $L2_1$-structured Cr_2YSn, with a 97.71 % spin polarization and a total moment of 4.99 μ_B/f.u. We observe that the total number of valence electrons for Cr_2YSn is 29 (Cr_1= 6, Cr_2=6, Y=3, Sn=14), following closely the standard $L2_1$ Slater-Pauling rule (M = N-24 = 29–24 = 5 ≈ 4.99). Cr_2YSn's high spin polarization makes it a promising half-metal candidate with potential applications in spintronics and novel spin-injection devices, should it be experimentally stabilized in the $L2_1$ phase [2]. The rest of the materials investigated maintain a spin polarization of less than 90 %, and do not show strict accordance with either the M = N-24 or the M = N-18 Slater-Pauling rules, as is expected [97,98].

3.3.2. DOS and PDOS

For the sake of clarity, all movement of DOS and PDOS peaks will be discussed in relation to the Fermi energy (represented by 0 eV on all DOS and PDOS graphs for simplicity). Due to tetrahedral crystal field splitting, the *d*-orbital PDOS data for each atom is further decomposed into three anti-bonding t_{2g} "triplet" orbitals (d_{xy}, d_{yz}, and d_{zx}) and two bonding e_g "doublet" orbitals (d_{z^2} and $d_{x^2-y^2}$). For further information on these orbitals the reader is referred to Graf et al. or Law et al. [53,99]. In our calculations the three triplet orbitals produce identical PDOS data. Likewise, the two doublet orbitals produce identical PDOS data which are distinct from the triplet states. In the following discussion the reported triplet (doublet) data is therefore the sum of the three (two) PDOS spectra which form the totality of the triplet (doublet) states in question.

Full Heusler

Given the preference of $L2_1$ structural phases throughout the majority of this series, special attention will be given to the electronic structure of those materials. DOS data for the A_2YSn-XA alloys can be found in Appendix A and the associated Data in Brief article [78]. At the beginning of the A-site period (A = Sc, Ti), there are corresponding sharp and broader peaks in both spin channels in the DOS plots (see Fig. 7). We note that there is a change in vertical scale for Fig. 7, Figs. 8, and 9. For reference, the sharper peaks in question are marked with a blue star. From the corresponding PDOS graphs, it is evident that the large sharper peaks (marked by a star) are comprised of A_1 and A_2 doublet states, while the broader peaks are generally comprised of A_1, A_2, and B triplet states. This indicates an expected strong hybridization between A-sites due to their near-identical chemical environments. It also indicates a hybridization of yttrium orbitals with A orbitals.

At A = V, the corresponding majority spin spikes shift down in energy and continue to shift down in energy as the number of valence electrons increase; this trend continues through the series until A = Ni. At A = Co the minority spin DOS spikes begin to shift down in energy, realigning with the majority spin DOS spikes at A = Ni. In previous sections we saw strong A-site magnetic moments appear and disappear along this same interval, as well as the anti-alignment of the yttrium moment. This can be explained through the interaction of triplet states between these sites. As shown in Figs. 7 and 8, these states tend to have the highest relative occupation and, given the offset between the spin channels, generate a relative spin moment, contributing to the high site-specific magnetic moments. Thus, this spin state asymmetry leads to more adjacent site interaction between orbitals, which drives the

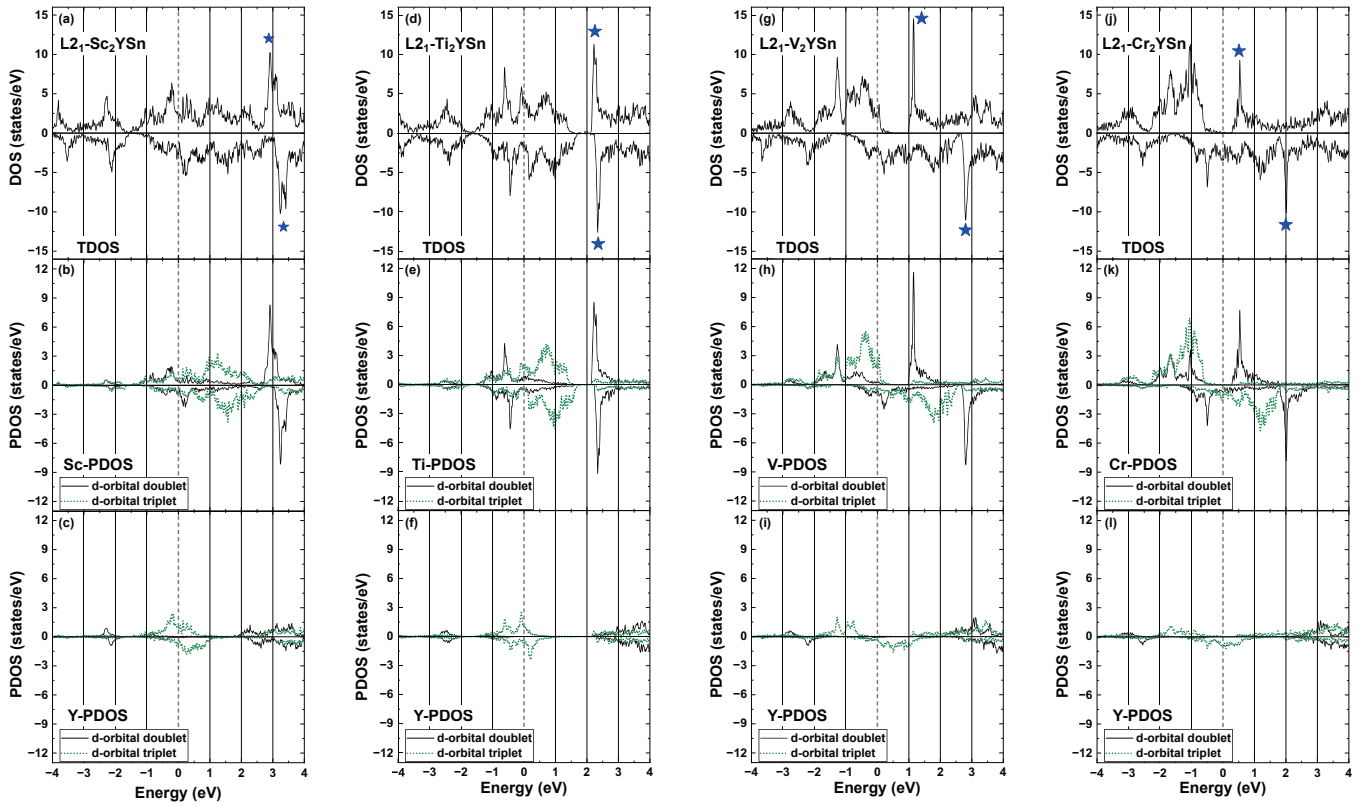

Fig. 7. Total density of states (TDOS), A-site *d*-orbital projected density of states (PDOS), and yttrium site *d*-orbital PDOS for (a)-(c) Sc_2YSn-$L2_1$, (d)-(f) Ti_2YSn-$L2_1$, (g)-(i) V_2YSn-$L2_1$, and (j)-(l) Cr_2YSn-$L2_1$. TDOS peaks of interest are marked with a blue star.

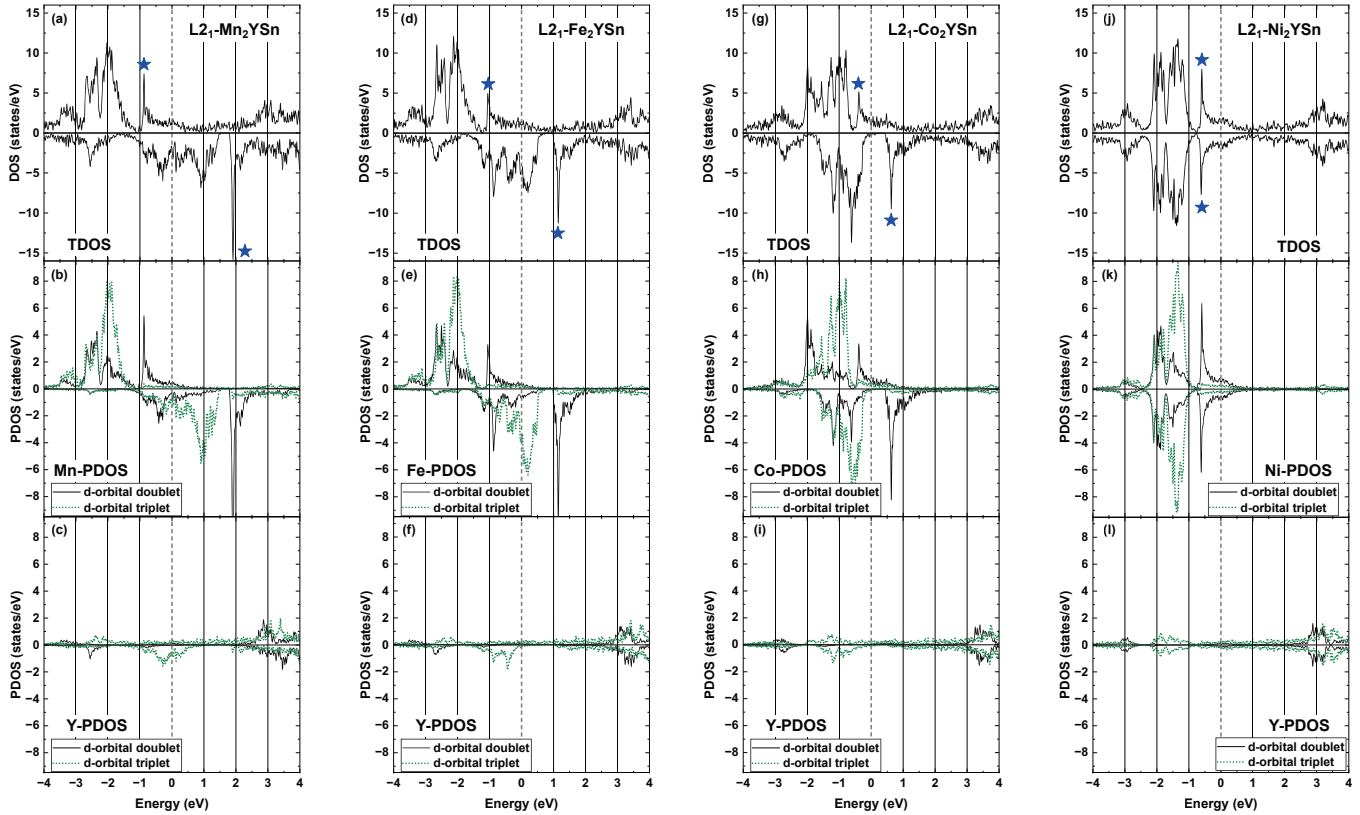

Fig. 8. Total density of states (TDOS), A-site projected *d*-orbital density of states (PDOS), and yttrium site *d*-orbital PDOS for (a)-(c) Mn_2YSn-$L2_1$, (d)-(f) Fe_2YSn-$L2_1$, (g)-(i) Co_2YSn-$L2_1$, and (j)-(l) Ni_2YSn-$L2_1$. TDOS peaks of interest are marked with a blue star.

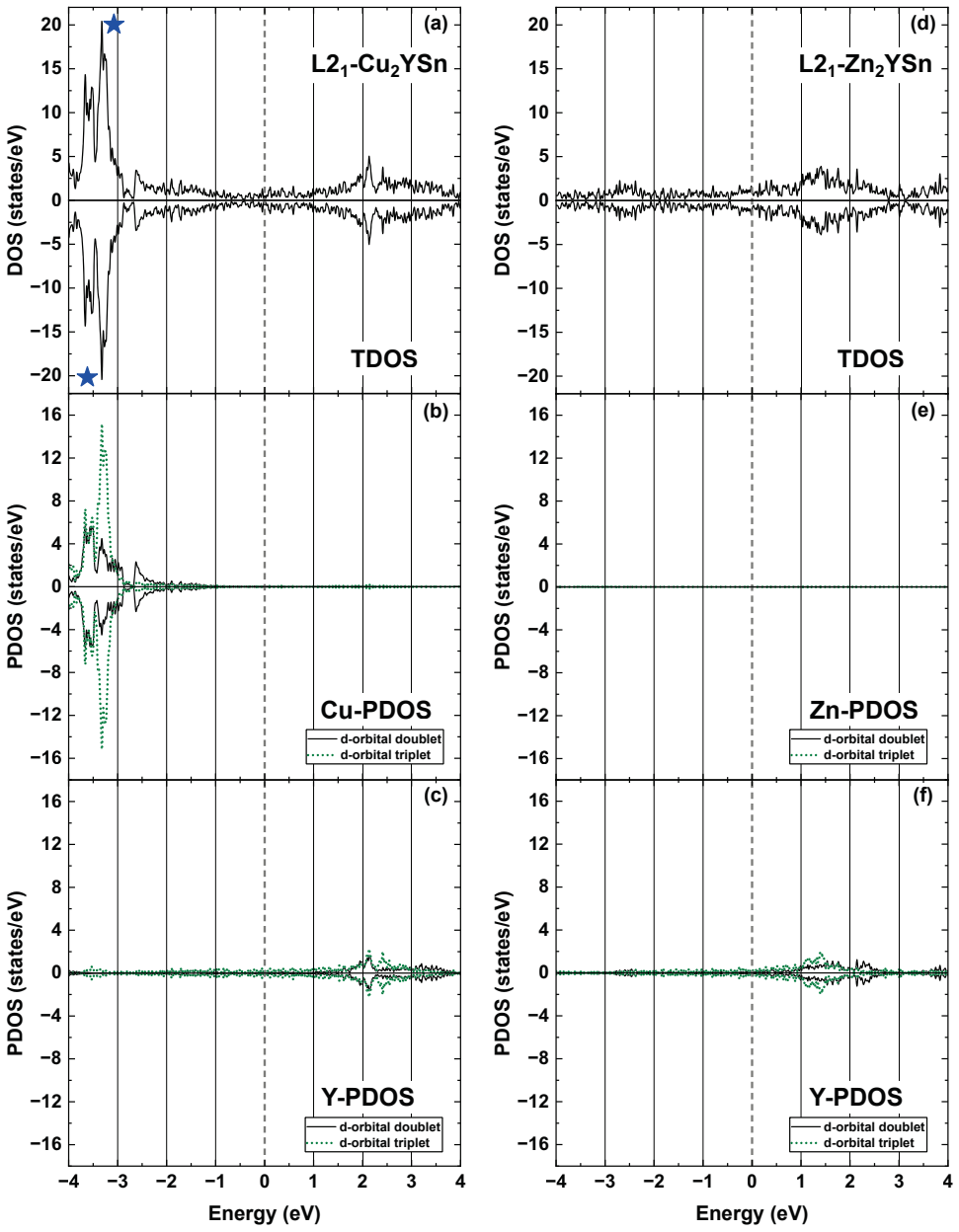

Fig. 9. Total density of states (TDOS), A-site projected *d*-orbital density of states (PDOS), and yttrium site *d*-orbital PDOS for (a)-(c) Cu_2YSn-$L2_1$ and (d)-(f) Zn_2YSn-$L2_1$. TDOS peaks of interest are marked with a blue star.

magnetic moment trend seen in previous sections. Further, these interactions are all driven by the partial filling of the *d*-orbitals on the A-sites, as can be seen clearly by the lack of interaction when these orbitals are mostly empty or full. We also see an overlap between the doublet (and occasionally triplet) peaks in the A-site and triplet peaks in the B-site (yttrium) PDOS graphs in Figs. 7, 8, and 9, which indicates a hybridization of these particular orbitals. For A = Cr, Mn, Fe, and Co, this hybridization tends to be accompanied by higher absolute spin polarization. These qualities indicate a possibility for electronic structure tuning in these materials, as half-metallicity is often driven by *d*-*d* hybridization between the A and B site in Heusler materials [94].

After this asymmetric shifting, the peaks realign at A = Ni and shift down in energy together for the rest of the series (see Figs. 8 and 9). This combined lowering in energy of both spin states after Ni is indicative of the Fermi energy increasing as the number of *d* electrons increases and is thus expected for the system. The disappearance of the spin-asymmetry of the DOS is coupled with the filling of the *d*-orbital on the A_1 and A_2 site, as well as the disappearance of strong magnetic moments within the system. Finally in Fig. 9(e) the Zn_2YSn-$L2_1$*d*-orbital PDOS is negligible within ± 4 eV of the Fermi energy for both the triplet and doublet states. This is because the high intensity DOS peaks (marked with blue stars) have moved below the chosen cutoff of −4 eV with respect to the Fermi energy, adopting a much stronger valence band character than those peaks in Figs. 7 and 8.

Inverse Heusler

Similarly to the $L2_1$ alloys, the XA DOS structures begin with corresponding peaks in both the majority and minority spin channels (see Figure B.10). These peaks are significantly less sharp than those in the $L2_1$ materials, indicating less well-defined hybridization states. However, at A = Cr the majority DOS peaks shift downward in energy (relative to the Fermi energy), creating an uneven DOS in terms of spin channel. At A = Co, the minority spin channel DOS peaks move downward too and begin to realign with the majority channel. After A = Ni, the total DOS shifts downward in energy due to the shifting Fermi

energy caused by increasing the number of electrons in the system. Again, this interesting trend of spin-asymmetric DOS peaks is mostly likely a result of an asymmetric filling of orbitals, caused by high spin states within the orbital scheme, leading to a high magnetic moment on each site. Given the lack of corresponding peaks within the A and B site PDOS, this indicates a lack of strong hybridization between these sites.

From A = Cr through A = Co, the orbitals are asymmetrically filled, leading to a high spin polarization in Co_2YSn. However, this is not due to the main peaks localized at −1.5 eV in the minority spin channel and −2.5 eV in the majority spin channel, but by a smaller peak in the minority spin channel at the Fermi energy and the lack of a corresponding peak in the other spin channel. In regard to the A_2YSn-XA band structures, the most notable feature is the emergence of a prominent flat band in Cu_2YSn-XA, something not seen in any of the $L2_1$ type materials (see Figure B.13). Flat band structures are indicative of highly localized electron orbitals such that the effective mass is nearly infinite, and can lead to interesting transport phenomena [100–103]. While we note that our calculations suggest that these XA phases are not energetically favored compared to their $L2_1$ counterpart, the differences between phases are in many cases smaller or comparable (see Fig. 4) to the energies available during experimental synthesis (0.1–0.3 eV/atom). Thus, the results reflect potential routes to interesting properties, especially with the inherent uncertainty in our theoretical model used.

4. Conclusion

In this study, phase preference and electronic structure of A_2YSn (A = Sc, Ti, V, Cr, Mn, Fe, Co, Ni, Cu, Zn) Heusler alloys were investigated using first principles density functional theory techniques. Calculations were performed in the Quantum Espresso 6.8 open-source package using the PAW method with a GGA scheme. Cohesive energies were determined for both the inverse Heusler XA and full Heusler $L2_1$ structures, revealing a phase preference transition from XA to $L2_1$ ordering at the A = V to A = Cr crossover. The final SCF calculations confirmed the A-site transition metal to be the dominant contributor to the total moment of those A_2YSn alloys with notable magnetic properties. Trends in the site-specific moments show the emergence of a ferrimagnetic coupling of the yttrium sublattice with the A element transition metal, matching observations reported in the literature for yttrium-based Heusler alloys.

Electronic structure calculations of these materials only reveal two possible half-metallic ferromagnets: Cr_2YSn-$L2_1$ and Co_2YSn-XA (however only Cr_2YSn-$L2_1$ is structurally favored). We predict Cr_2YSn-$L2_1$ possesses a spin polarization of 97.71 % and a half-metallic gap of 0.109 eV. Overall, a trend was observed in which the partial filling of the *d*-orbitals on the A-sites led to notable interactions between doublet and triplet states on the A and B sites respectively. These interactions contributed to the magnetic moment trends discussed above. The asymmetric shifting of DOS peaks between the spin channels that indicated this trend also demonstrate a possibility of half-metallic design through substitutional doping of these materials.

Predicted phase preference for each alloy was compared against data from the online quantum materials database (OQMD) (see Appendix A), finding good agreement regarding the relative stability of the full and inverse Heusler structures predicted by our calculations. Future studies investigating the role of competing C1b (half-Heusler) structures, as well as binary phase decomposition, could complement nicely the data reported here. Overall, these results offer unique insight into structural ordering and electronic structure of yttrium-based Heusler alloys, which can inform future spintronic and ferrimagnetic materials applications.

CRediT authorship contribution statement

Adam J. Hauser: Writing – review & editing, Writing – original draft, Supervision, Project administration, Methodology, Investigation, Funding acquisition, Formal analysis, Conceptualization. **Justin Lewis:** Writing – review & editing, Investigation. **Ridwan Nahar:** Writing – review & editing, Supervision, Investigation, Formal analysis, Data curation. **Ka Ming Law:** Writing – review & editing, Supervision, Investigation, Formal analysis. **Thomas Roden:** Writing – review & editing, Investigation. **Riley Nold:** Writing – review & editing, Writing – original draft, Investigation, Formal analysis, Data curation, Conceptualization. **Michael Zengel:** Writing – review & editing, Writing – original draft, Investigation, Formal analysis, Data curation, Conceptualization.

Declaration of Competing Interest

The authors declare the following financial interests/personal relationships which may be considered as potential competing interests: Adam Hauser reports financial support was provided by National Science Foundation. Riley Nold reports financial support was provided by National Science Foundation. Michael Zengel reports financial support was provided by National Science Foundation. Ridwan Nahar reports financial support was provided by National Science Foundation. Justin Lewis reports financial support was provided by National Science Foundation. If there are other authors, they declare that they have no known competing financial interests or personal relationships that could have appeared to influence the work reported in this paper.

Data availability

The data not provided here is in a cited Data in Brief, already published. Anything else can be furnished upon request.

Acknowledgments

The authors gratefully acknowledge financial support from the National Science Foundation (NSF CAREER DMR-2047251). A.J.H. thanks K.Q. Twon for useful conversations and diversions.

Appendix A. Competing Structures

Although $L2_1$ and XA are taken to be the dominant phases in this study, other competing phases exist. This includes ternary alloys of other space groups, binary material systems, and the constituent elements. It is therefore worthwhile to briefly discuss the broader range of competing phases which may be observed for A_2YSn type Heusler alloys. To this end, we compare the phase stability results of this study against theoretical phase diagram information taken from the Open Quantum Materials database (OQMD) [104,105]. Such comparisons play an important role in verifying the validity of our computational approach within the broader collection of existing computational and experimental data on A_2YSn alloys. Table A.2 lists the competing species and the distance from the convex hull (eV/atom) for each A_2YSn alloy and phase ($L2_1$ and XA) taken from OQMD. Despite potential issues of incomplete or incorrect thermodynamic data, OQMD serves as a good guide for general observations.

Each alloy in this study is reported by OQMD to have a positive convex hull distance, suggesting the existence of competing species within the compositional phase space. However, a positive hull distance should not be taken to indicate the experimental infeasibility of manufacturing A_2YSn Heusler alloys. For example, the prototypical $L2_1$ Heusler alloy Cu_2MnAl studied by F. Heusler in 1903 is listed with a convex hull distance of 0.06 eV/atom, yet is experimentally stable in both bulk and thin film settings [20,106,107]. This indicates that the experimental parameters of sample

manufacturing, such as operating pressure and temperature, growth atmosphere, thin film vs. bulk setting, etc., can stabilize phases which may have an otherwise positive convex hull distance. It is also possible that the phase with the lowest free energy during manufacturing (which occurs well above 0 K in most cases) is different than that phase which is predicted by our (and OQMD's) DFT calculations, since such calculations assume a zero-kelvin environment.

Table A.2
Convex hull distance (eV/atom) and competing phases reported from Open Quantum Materials Database for both $L2_1$ and XA phases of A_2YSn Heusler alloys (A = Sc, Ti, V, Cr, Mn, Fe, Co, Ni, Cu, and Zn).

Alloy	Phase	Convex Hull Distance (eV/atom)	Competing Phases (OQMD)
Sc_2YSn	$L2_1$	0.255	Sc, Sc_5Sn_3, Y_5Sn_3
Sc_2YSn	XA	0.233	Sc, Sc_5Sn_3, Y_5Sn_3
Ti_2YSn	$L2_1$	0.368	Ti, Ti_3Sn, Y_5Sn_3
Ti_2YSn	XA	0.324	Ti, Ti_3Sn, Y_5Sn_3
V_2YSn	$L2_1$	0.606	V, YSn
V_2YSn	XA	0.608	V, YSn
Cr_2YSn	$L2_1$	0.583	Cr, YSn
Cr_2YSn	XA	0.898	Cr, YSn
Mn_2YSn	$L2_1$	0.405	Mn, YSn
Mn_2YSn	XA	0.504	Mn, YSn
Fe_2YSn	$L2_1$	0.368	Fe, YSn
Fe_2YSn	XA	0.452	Fe, YSn
Co_2YSn	$L2_1$	0.141	Co, YSn
Co_2YSn	XA	0.601	Co, YSn
Ni_2YSn	$L2_1$	0.065	NiYSn, Ni_3Sn_2, Ni_5Y
Ni_2YSn	XA	0.425	NiYSn, Ni_3Sn_2, Ni_5Y
Cu_2YSn	$L2_1$	0.098	Cu, CuYSn
Cu_2YSn	XA	0.305	Cu, CuYSn
Zn_2YSn	$L2_1$	0.254	ZnYSn, YSn_2, $Zn_{17}Y_2$
Zn_2YSn	XA	0.322	ZnYSn, YSn_2, $Zn_{17}Y_2$

Furthermore, differences in the OQMD-reported convex hull distance between the individual phases ($L2_1$ and XA) can serve as a second metric of preferential phase ordering, similar to the role that the difference in cohesive energies (ΔE) plays in our calculations. We will refer to this new metric as the OQMD phase preference. For each alloy reported, the phase with the lower OQMD convex hull distance matches the preferred phase predicted by our calculations (based upon the value of ΔE for the alloy), with the exception of V_2YSn, as shown in Table A.3. This supports the accuracy of the calculated cohesive energy values and the determinations of relative $L2_1$/XA phase stability for the A_2YSn alloys studied.

Table A.3
Phase preference metric calculated from OQMD's convex hull distances and ΔE from this report's DFT calculations. A positive number indicates an XA preference, while a negative number indicates an $L2_1$ preference.

Alloy	OQMD Phase Preference (eV/atom)	DFT Phase Preference: ΔE (eV/atom)
Sc_2YSn	0.002	0.021438
Ti_2YSn	0.044	0.056071
V_2YSn	−0.002	0.009110
Cr_2YSn	−0.315	−0.395258
Mn_2YSn	−0.099	−0.094349
Fe_2YSn	−0.084	−0.076897
Co_2YSn	−0.046	−0.374110
Ni_2YSn	−0.36	−0.310577
Cu_2YSn	−0.207	−0.207711
Zn_2YSn	−0.068	−0.071413

To note, V_2YSn is found to have both a small ΔE as well as a small difference in convex hull distance between the phases. Therefore, this particular discrepancy may be the result of the different computational methods used combined with the relatively low stability of the preferred V_2YSn phase against site-swap disorder. We also observe for Co_2YSn a noticeable discrepancy between the magnitudes of the reported ΔE and the OQMD "phase preference" value. This discrepancy may arise from differing treatments of the Co_2YSn magnetic moments, in particular the use of a scalar relativistic approach as opposed to the more complex full relativistic scheme.

Aside from decomposition into the constituent elements, the YSn binary phase is listed as a competing species for many of the 3*d* A_2YSn materials. In addition, the half-Heusler C1b structure is noted as a competing phase for the Ni_2YSn, Cu_2YSn, and Zn_2YSn alloys. Therefore, further investigations into the stability of A_2YSn Heuslers against half-Heusler, binary, and elemental decomposition would provide additional insight to the atomic ordering data produced here.

B. A_2YSn $L2_1$ and XA Band Structures

Although the DOS and PDOS data for the A_2YSn system were of primary interest, for completeness we report the electronic band structures for each compound in both the $L2_1$ and XA phases. Data for Sc_2YSn-$L2_1$ through Mn_2YSn-$L2_1$ can be found in Figure B.10, whereas Fe_2YSn-$L2_1$ through Zn_2YSn-$L2_1$ are illustrated in Figure B.11. The corresponding band structures for the XA phases can be found in Figures B.12 and B.13.

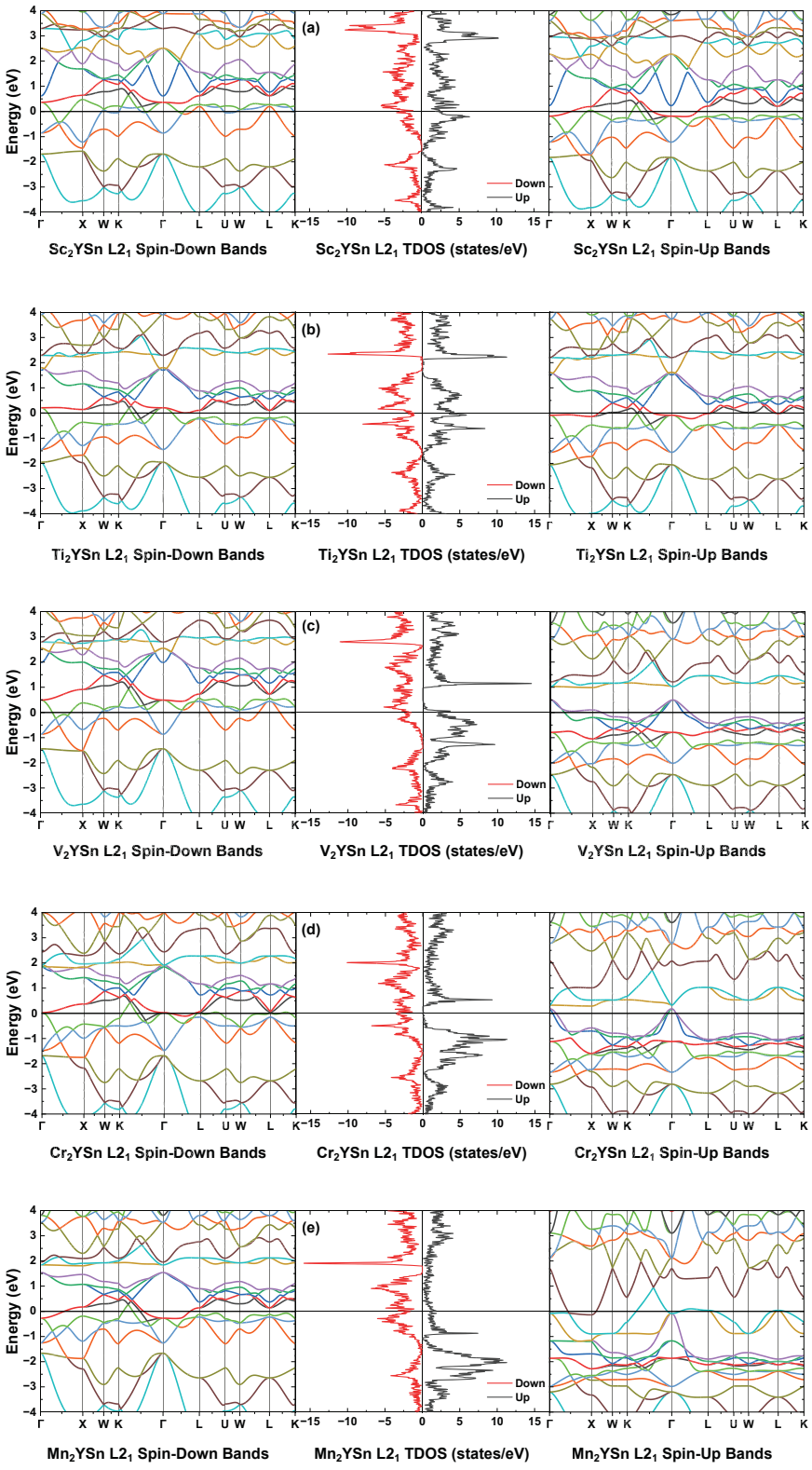

Fig. B.10. Total electronic density of states in comparison to spin-up and spin-down band structures within ± 4 eV range of the Fermi energy. Data is included for (a) $Sc_2YSn\text{-}L2_1$, (b) $Ti_2YSn\text{-}L2_1$, (c) $V_2YSn\text{-}L2_1$, (d) $Cr_2YSn\text{-}L2_1$, (e) and $Mn_2YSn\text{-}L2_1$.

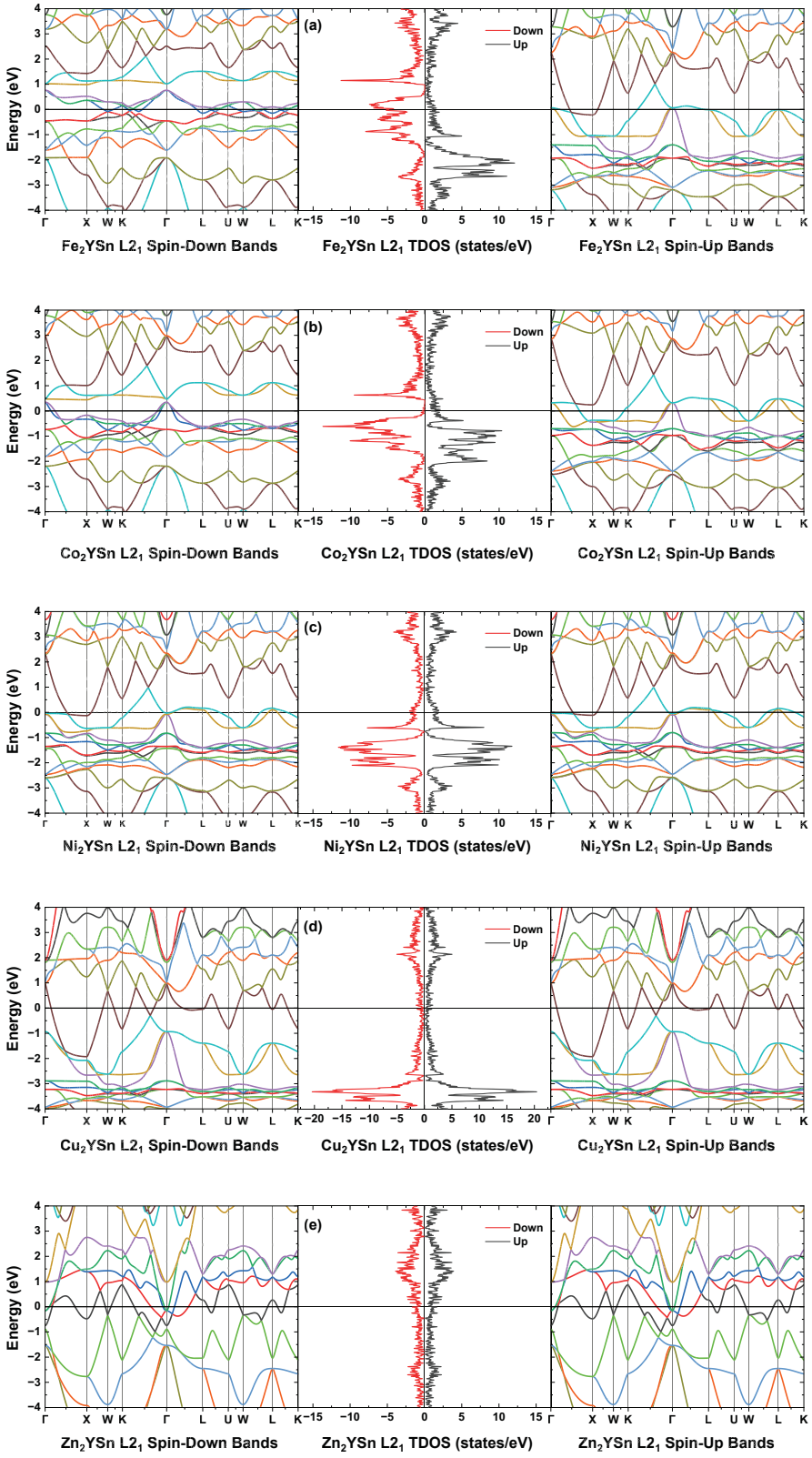

Fig. B.11. Total electronic density of states in comparison to spin-up and spin-down band structures within ± 4 eV range of the Fermi energy. Data is included for (a) Fe_2YSn-$L2_1$, (b) Co_2YSn-$L2_1$, (c) Ni_2YSn-$L2_1$, (d) Cu_2YSn-$L2_1$, (e) and Zn_2YSn-$L2_1$.

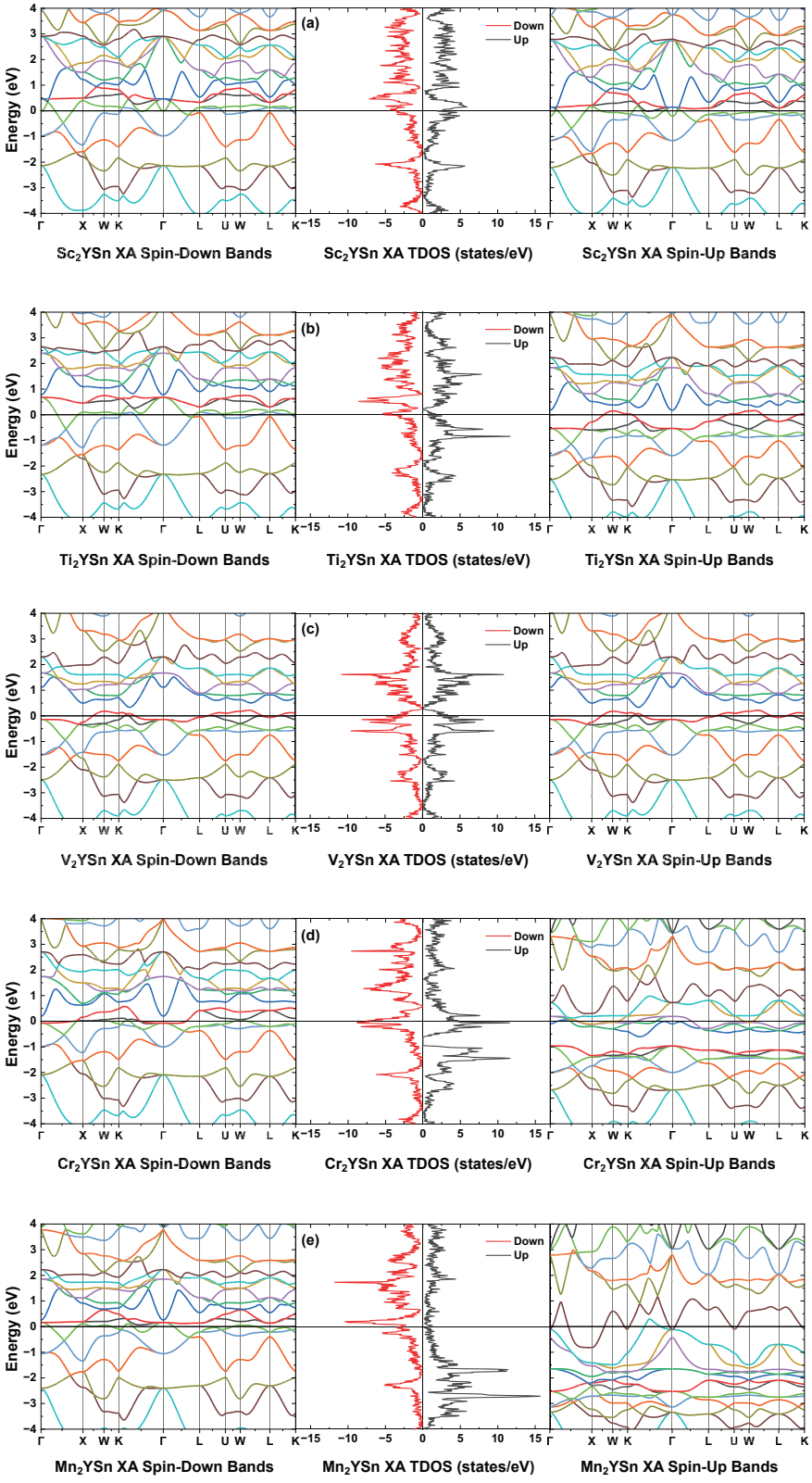

Fig. B.12. Total electronic density of states in comparison to spin-up and spin-down band structures within ± 4 eV range of the Fermi energy. Data is included for (a) Sc_2YSn-XA, (b) Ti_2YSn-XA, (c) V_2YSn-XA, (d) Cr_2YSn-XA, (e) and Mn_2YSn-XA.

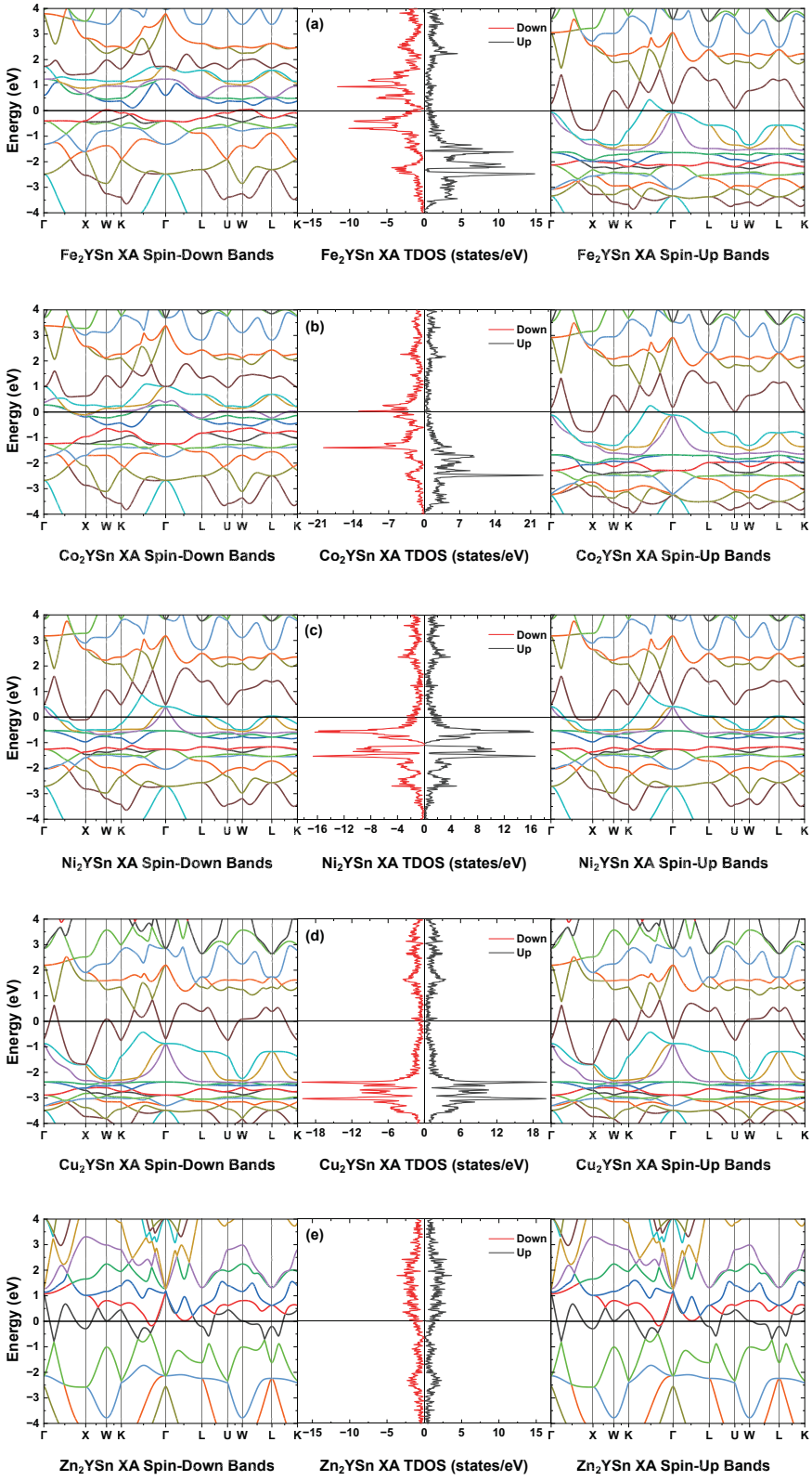

Fig. B.13. Total electronic density of states in comparison to spin-up and spin-down band structures within ± 4 eV range of the Fermi energy. Data is included for (a) Fe_2YSn-XA, (b) Co_2YSn-XA, (c) Ni_2YSn-XA, (d) Cu_2YSn-XA, (e) and Zn_2YSn-XA.

The high intensity DOS peaks noted previously in Figures 7, Figures 8, and 9 correspond to a high-density band region which moves downward in energy with increasing A-site valency. The PDOS data in Figures 7, Figures 8, and 9 indicate this high-density band region to be comprised primarily of A-site *d*-orbital doublet and triplet states. In particular, the flat band observed in Figure B.13(d) is similarly comprised of such A-site *d*-orbital states. This reinforces the important role that A-site valency plays in determining the electronic character of A_2YSn Heuslers, and indicates the possibility of A_2YSn band engineering through substitutional doping or other means of stoichiometric manipulation.

For Zn_2YSn-$L2_1$ and Zn_2YSn-XA (Figures B.11(e) and B.13(e)), the dense band region observed for the other structures disappears below the −4 eV energy cutoff, continuing the general downward trend of the prominent DOS peaks. In particular the Zn_2YSn-$L2_1$ data in Figure B.11(d) corresponds nicely with the disappearance of the Zn *d*-orbital PDOS in Figure 9(e).

Despite the inherent limitations of *ab-initio* modeling, these data reinforce the exciting electronic properties of the A_2YSn system and motivate future studies into yttrium-based Heuslers more broadly.

References

[1] P. Alhan, R. Dholpuria, A. Rani, R. Kumar, Effect of strain on the spin-polarization, mechanical and magnetic properties of Co_2 TiGe Heusler alloy: a first principle study, Mem. - Mater., Devices, Circuits Syst. 4 (2023) 100046.

[2] I. Galanakis, Slater-Pauling behavior in half-metallic Heusler compounds, Nanomaterials 13 (2023) 2010.

[3] M. Obaida, L. Galdun, T. Ryba, V. Komanicky, K. Saksl, M. Durisin, J. Kovac, V. Haskova, P. Szabo, Z. Vargova, R. Varga, Spin polarization in Cu_2 MnSn Heusler alloy produced by melt-spinning, Intermetallics 85 (2017) 139–143.

[4] M. Mokhtari, F. Dahmane, L. Zekri, S. Benalia, N. Zekri, Ab initio investigation of structural stability and electronic and magnetic properties of the half-Heusler alloys: MTiSb (M = Fe, Co, and Ni), J. Supercond. Nov. Magn. 31 (2018) 2991–2998.

[5] A. Zerouali, A. Mokaddem, B. Doumi, F. Dahmane, M. Elkeurti, A. Sayede, A. Tadjer, First-principle calculations of electronic and ferromagnetic properties of Al_{1-x} V_x Sb, J. Comput. Electron. 15 (2016) 1255–1262.

[6] A. Chanda, D. Rani, D. DeTellem, N. Alzahrani, D.A. Arena, S. Witanachchi, R. Chatterjee, M.-H. Phan, H. Srikanth, Large thermo-spin effects in Heusler alloy-based spin gapless semiconductor thin films, ACS Appl. Mater. Interfaces 15 (2023) 53697–53713.

[7] V.V. Marchenkov, V.Y. Irkhin, Magnetic states and electronic properties of manganese-based intermetallic compounds Mn_2 YAl and Mn_3 Z (Y = V, Cr, Fe, Co, Ni; Z = Al, Ge, Sn, Si, Pt), Materials 16 (2023) 6351.

[8] X. Wang, Z. Cheng, J. Wang, X.-L. Wang, G. Liu, Recent advances in the Heusler based spin-gapless semiconductors, J. Mater. Chem. C 4 (2016) 7176–7192.

[9] T. Bachaga, J. Zhang, M. Khitouni, J.J. Sunol, NiMn-based Heusler magnetic shape memory alloys: a review, Int. J. Adv. Manuf. Technol. 103 (2019) 2761–2772.

[10] Y. Shen, Z. Wei, W. Sun, Y. Zhang, E. Liu, J. Liu, Large elastocaloric effect in directionally solidified all-d-metal Heusler metamagnetic shape memory alloys, Acta Mater. 188 (2020) 677–685.

[11] K. Zhang, C. Tan, E. Guo, Z. Feng, J. Zhu, Y. Tong, W. Cai, Simultaneous tuning of martensitic transformation behavior, magnetic and mechanical properties in Ni-Mn-Sn magnetic alloy by Cu doping, J. Mater. Chem. C 6 (2018) 5228–5238.

[12] Z. Gui, G. Wang, H. Wang, Y. Zhang, Y. Li, X. Wen, Y. Li, K. Peng, X. Zhou, J. Ying, X. Chen, Large improvement of thermoelectric performance by magnetism in Co-based full-Heusler alloys, Adv. Sci. 10 (2023) 2303967.

[13] B. Hinterleitner, I. Knapp, M. Poneder, Y. Shi, H. Müller, G. Eguchi, C. Eisenmenger-Sittner, M. Stöger-Pollach, Y. Kakefuda, N. Kawamoto, Q. Guo, T. Baba, T. Mori, S. Ullah, X.-Q. Chen, E. Bauer, Thermoelectric performance of a metastable thin-film Heusler alloy, Nature 576 (2019) 85–90.

[14] A. Ojha, R.K. Sabat, S. Bathula, Advancement in half-Heusler thermoelectric materials and strategies to enhance the thermoelectric performance, Mater. Sci. Semicond. Process. 171 (2024) 107996.

[15] K. Hamaya, M. Yamada, Semiconductor spintronics with Co_2 -Heusler compounds, MRS Bull. 47 (2022) 584–592.

[16] N. Maji, T.K. Nath, Demonstration of reconfigurable magnetic tunnel diode and giant tunnel magnetoresistance in magnetic tunnel junctions made with spin gapless semiconductor and half-metallic Heusler alloy, Appl. Phys. Lett. 120 (2022) 072401.

[17] A. Mahendra, P.P. Murmu, S.K. Acharya, A. Islam, H. Fiedler, P. Gupta, S. Granville, J. Kennedy, Shaping perpendicular magnetic anisotropy of Co_2 MnGa Heusler alloy using ion irradiation for magnetic sensor applications, Sensors 23 (2023) 4564.

[18] K. Ahn, Ni-Mn based conventional full Heusler alloys, all-d-metal full Heusler alloys, and their promising functional properties to solid state cooling by magnetocaloric effect, J. Alloy. Compd. 978 (2024) 173378.

[19] L. Zhang, J. Zhang, K. Li, L. He, C. Zhou, D. Wang, S. Yang, S. Li, D. Wang, Magnetic glassy martensite induced reversible magnetocaloric effect in Heusler alloys, Acta Mater. 239 (2022) 118245.

[20] F. Heusler, Über die synthese ferromagnetischer manganlegierungen, Verh, Dtsch. Phys. Ges. 5 (1903) 219–223.

[21] F. Heusler, W. Starck, E. Haupt, Magnetisch-chemische studien, Verh. Dtsch. Phys. Ges. 5 (1903) 219–232.

[22] Y. Feng, S. Zhang, Q. Zeng, M. Lyu, J. Liu, J. Yang, Y. Wang, Q. Ren, Y. Liu, B. Wang, H. Wei, E. Liu, Evolution of structure, magnetism, and electronic/thermal-transports of Ti(Cr)-substituted Fe_2 CrV all-d-metal Heusler ferromagnets, J. Alloy. Compd. 1003 (2024) 175660.

[23] S. Kc, R. Mahat, S. Regmi, A. Mukherjee, P. Padhan, R. Datta, W.H. Butler, A. Gupta, P. LeClair, Tunable properties and potential half-metallicity in (Co_{2-x} Ti_x)FeGe Heusler alloys: An experimental and theoretical investigation, Phys. Rev. Mater. 3 (11) (2019) 114406.

[24] Y. Zhang, J. Bai, K. Guo, D. Liu, J. Gu, N. Morley, Q. Ma, Q. Gao, Y. Zhang, C. Esling, X. Zhao, L. Zuo, An alloying strategy for tuning magnetism, thermal hysteresis, and mechanical properties in Ni-Mn-Sn-based Heusler alloys, J. Alloy. Compd. 979 (2024) 173593.

[25] I. Galanakis, P.H. Dederichs, N. Papanikolaou, Slater-Pauling behavior and origin of the half-metallicity of the full-Heusler alloys, Phys. Rev. B 66 (17) (2002).

[26] R. Gavrea, A. Bolinger, V. Pop, O. Isnard, M. Coldea, D. Benea, Influence of Cu doping on the electronic structure and magnetic properties of the Mn_2 VAl Heusler compound, Phys. Status Solidi (b) 254 (11) (2017) 1700160.

[27] N.A. Zarkevich, P. Singh, A.V. Smirnov, D.D. Johnson, Effect of substitutional doping and disorder on the phase stability, magnetism, and half-metallicity of Heusler alloys, Acta Mater. 225 (2022) 117477.

[28] S.K. Kim, G.S.D. Beach, K.-J. Lee, T. Ono, T. Rasing, H. Yang, Ferrimagnetic spintronics, Nat. Mater. 21 (1) (2022) 24–34.

[29] M. Ishikawa, J.-L. Jorda, A. Junod, New ternary superconductors of the YPd_2 Sn-type, In: Superconductivity in d- and f-Band Metals, edited by W. Buckel and W. Weber (Kernforschungszentrum, Karlsruhe), 1982, 141.

[30] J.H. Wernick, G.W. Hull, T.H. Geballe, J.E. Bernardini, J.V. Waszczak, Superconductivity in ternary Heusler intermetallic compounds, Mater. Lett. 2 (2) (1983) 90–92.

[31] T. Klimczuk, C.H. Wang, K. Gofryk, F. Ronning, J. Winterlik, G.H. Fecher, J. C. Griveau, E. Colineau, C. Felser, J.D. Thompson, D.J. Safarik, R.J. Cava, Superconductivity in the Heusler family of intermetallics, Phys. Rev. B 85 (17) (2012) 174505.

[32] H. Saadaoui, T. Shiroka, A. Amato, C. Baines, H. Luetkens, E. Pomjakushina, V. Pomjakushin, J. Mesot, M. Pikulski, E. Morenzoni, μ SR and NMR study of the superconducting Heusler compound YPd_2 Sn, Phys. Rev. B 88 (9) (2013) 094518.

[33] H.M. Tütüncü, G.P. Srivastava, Phonon anomalies and superconductivity in the Heusler compound YPd_2 Sn, J. Appl. Phys. 116 (1) (2014) 013907.

[34] S.K. Malik, A.M. Umarji, G.K. Shenoy, Depression of the superconducting transition temperature of the Heusler alloy Pd_2 YSn with the addition of magnetic rare-earth metals, Phys. Rev. B 32 (7) (1985) 4426–4430.

[35] A.M. Umarji, S.K. Malik, G.K. Shenoy, Effect of paramagnetic rare earth ions on the superconducting transition temperature of the Heusler alloy Pd_2 YSn, Phys. B +C 135 (1) (1985) 423–425.

[36] J.L. Jorda, M. Ishikawa, J. Muller, Phase equilibria and superconductivity in the Pd_2 YSn system, J. Less Common Met. 107 (2) (1985) 321–330.

[37] M.J. Besnus, J.P. Kappler, M.F. Ravet, A. Meyer, R. Lahiouel, J. Pierre, E. Siaud, G. Nieva, J. Sereni, Structural and magnetic properties of the ternary rare earth (RE) compound series $REInAu_2$ (RE = La to Lu, Y), J. Less Common Met. 120 (1) (1986) 101–112.

[38] M.J. Besnus, M. Benakki, J.P. Kappler, P. Lehmann, A. Meyer, P. Panissod, Low temperature properties of the new Heusler phase $UInAu_2$: magnetic to non-magnetic transition in (U,Y)$InAu_2$ and (U,Th)$InAu_2$, J. Less Common Met. 141 (1) (1988) 121–131.

[39] A.E. Dwight, C.W. Kimball, ScT_2 X and LnT_2 X compounds with the $MnCu_2$ Al-type structure, J. Less Common Met. 127 (1987) 179–182.

[40] M. Johnscher, S. Stein, O. Niehaus, C. Benndorf, L. Heletta, M. Kersting, C. Höting, H. Eckert, R. Pöttgen, Magnesium and Cadmium containing Heusler phases $REPd_2$ Mg, $REPd_2$ Cd, $REAg_2$ Mg, $REAu_2$ Mg and $REAu_2$ Cd, Solid State Sci. 52 (2016) 57–64.

[41] C. Benndorf, S. Stein, L. Heletta, M. Kersting, H. Eckert, R. Pöttgen, A 25Mg, 89Y and 115In solid state MAS NMR study of YT_2 X and $Y(T_{0.5}$ T' $_{0.5})_2$ X (T/T'= Pd, Ag, Au; X = Mg, In) Heusler phases, Dalton Trans. 46 (1) (2017) 250–259.

[42] Y. Yang, Z.-Y. Feng, J.-M. Zhang, Half-metallic behavior and magnetic properties of various (001) surfaces for the Heusler alloy Y_2 CrSn, J. Phys. Chem. Solids 131 (2019) 164–172.

[43] S. Yousuf, D.C. Gupta, Insight into half-metallicity, spin-polarization and mechanical properties of $L2_1$ structured MnY_2 Z (Z= Al, Si, Ga, Ge, Sn, Sb) Heusler alloys, J. Alloy. Compd. 735 (2018) 1245–1252.

[44] Y. Gupta, M.M. Sinha, S.S. Verma, Lattice dynamics of novel Heusler alloys MnY_2 Z (Z=Al and Si), Phys. B: Condens. Matter 590 (2020) 412222.

[45] S. Ghosh, S. Ghosh, Systematic understanding of half-metallicity of ternary compounds in Heusler and inverse Heusler structures with 3d and 4d elements, Phys. Scr. 94 (12) (2019) 125001.

[46] T. Burch, T. Litrenta, J. Budnick, Hyperfine studies of site occupation in ternary systems, Phys. Rev. Lett. 33 (1974) 421–424.

[47] V. Niculescu, T. Burch, K. Raj, J. Budnick, Properties of Heusler-type materials Fe_2 TSi and $FeCo_2$ Si, J. Magn. Magn. Mater. 5 (1977) 60–66.

[48] X.-H. Kang, J.-M. Zhang, First-principles study of the half-metallic and magnetic properties for new yttrium-based full-Heusler alloys Y_2 CrZ (Z = Al, Ga, In), Solid State Commun. 264 (2017) 19–25.

[49] O. Amrich, M.E.A. Monir, H. Baltach, S.B. Omran, X.-W. Sun, X. Wang, Y. Al-Douri, A. Bouhemadou, R. Khenata, Half-metallic ferrimagnetic characteristics of Co_2 YZ (Z = P, As, Sb, and Bi) new full-Heusler alloys: a DFT study, J. Supercond. Nov. Magn. 31 (1) (2018) 241–250.

[50] P.G.V. Engen, K.H.J. Buschow, M. Erman, Magnetic properties and magneto-optical spectroscopy of Heusler alloys based on transition metals and Sn, J. Magn. Magn. Mater. 30 (3) (1983) 374–382.

[51] T. Graf, C. Felser, Crystal structure of Heusler compounds. Spintronics: From Materials to Devices, Springer, Dordrecht, 2013, pp. 45–59.
[52] S. Tavares, K. Yang, M.A. Meyers, Heusler alloys: past, properties, new alloys, and prospects, Prog. Mater. Sci. 132 (2023).
[53] T. Graf, C. Felser, S.S.P. Parkin, Simple rules for the understanding of Heusler compounds, Prog. Solid State Chem. 39 (1) (2011) 1–50.
[54] S. Rauf, S. Arif, M. Haneef, B. Amin, The first principle study of magnetic properties of Mn_2 WSn, Fe_2 YSn (Y=Ti, V), Co_2 YSn (Y=Ti, Zr, Hf, V, Mn) and Ni_2 YSn (Y=Ti, Zr, Hf, V, Mn) Heusler alloys, J. Phys. Chem. Solids 76 (2015) 153–169.
[55] T. Graf, F. Casper, J. Winterlik, B. Balke, G.H. Fecher, C. Felser, Crystal structure of new Heusler compounds, Z. F. üR. Anorg. und Allg. Chem. 635 (6-7) (2009) 976–981.
[56] C. de Melo, C. Guillemard, A.M. Friedel, V. Palin, J.C. Rojas-Sánchez, S. Petit-Watelot, S. Andrieu, Unveiling transport properties of Co_2 MnSi Heusler epitaxial thin films with ultra-low magnetic damping, Appl. Mater. Today 25 (2021) 101174.
[57] A. Berche, M.T. Noutack, M.L. Doublet, P. Jund, Unexpected band gap increase in the Fe_2 VAl Heusler compound, Mater. Today Phys. 13 (2020) 100203.
[58] V. Sharma, P. Kumar, V. Sharma, B.K. Kuanr, Growth temperature-controlled Gilbert damping and anisotropies in PLD grown epitaxial Co_2 FeSi Heusler alloy thin film, AIP Adv. 13 (2) (2023) 025012.
[59] A. Shamardin, S. Cichoň, M. Rameš, E.D. Prado, L. Volfová, T. Kmječ, L. Fekete, J. Kopeček, P. Kos, L. Nowak, J. Heicl, J. Zázvorka, J. Hamrle, M. Veis, O. Heczko, J. Lančok, Growth and properties of full Heusler Co_2 TiSn epitaxial thin films, J. Alloy. Compd. 1002 (2024) 175296.
[60] H. Li, K. Hayashi, Y. Nagashima, S. Yoshioka, J. Dong, J.-F. Li, Y. Miyazaki, Effects of disorder on the electronic structure and thermoelectric properties of an inverse full-Heusler Mn_2 CoAl alloy, Chem. Mater. 33 (7) (2021) 2543–2547.
[61] S. Kurdi, Y. Sakuraba, K. Masuda, H. Tajiri, B. Nair, G.F. Nataf, M.E. Vickers, G. Reiss, M. Meinert, S.S. Dhesi, M. Ghidini, Z.H. Barber, Quantitative atomic order characterization of a Mn_2 FeAl Heusler epitaxial thin film, J. Phys. D: Appl. Phys. 55 (18) (2022) 185305.
[62] A. Wederni, J. Daza, W.B. Mbarek, J. Saurina, L. Escoda, J.-J. Suñol, Crystal structure and properties of Heusler alloys: a comprehensive review, Metals 14 (6) (2024) 688.
[63] Y. Venkateswara, D. Rani, K.G. Suresh, A. Alam, Half-metallic ferromagnetism and Ru-induced localization in quaternary Heusler alloy CoRuMnSi, J. Magn. Magn. Mater. 502 (2020) 166536.
[64] J. Kudrnovský, V. Drchal, S.K. Bose, I. Turek, Electronic and transport properties of a new quaternary Heusler alloy CoMnFeSi, Phys. Rev. B 97 (21) (2018) 214404.
[65] Y. Feng, H. Chen, H. Yuan, Y. Zhou, X. Chen, The effect of disorder on electronic and magnetic properties of quaternary Heusler alloy CoFeMnSi with LiMgPbSb-type structure, J. Magn. Magn. Mater. 378 (2015) 7–15.
[66] J. Ma, V.I. Hegde, K. Munira, Y. Xie, S. Keshavarz, D.T. Mildebrath, C. Wolverton, A.W. Ghosh, W.H. Butler, Computational investigation of half-Heusler compounds for spintronics applications, Phys. Rev. B 95 (2) (2017).
[67] H. Luo, Y. Xin, B. Liu, F. Meng, H. Liu, E. Liu, G. Wu, Competition of $L2_1$ and XA structural ordering in Heusler alloys X_2 CuAl (X = Sc, Ti, V, Cr, Mn, Fe, Co, Ni), J. Alloy. Compd. 665 (2016) 180–185.
[68] K. Mishra, P.A. Bhobe, Magnetic properties and identification of Griffiths-like phase in Mn_2 FeSi Heusler antiferromagnet, J. Alloy. Compd. 970 (2024) 172611.
[69] H.C. Kandpal, V. Ksenofontov, M. Wojcik, R. Seshadri, C. Felser, Electronic structure, magnetism and disorder in the Heusler compound Co_2 TiSn, J. Phys. D: Appl. Phys. 40 (6) (2007) 1587–1592.
[70] S.J. Ahmed, C. Boyer, M. Niewczas, Magnetic and structural properties of Co_2 MnSi based Heusler compound, J. Alloy. Compd. 781 (2019) 216–225.
[71] Y. Feng, J.Y. Rhee, T.A. Wiener, D.W. Lynch, B.E. Hubbard, A.J. Sievers, D. L. Schlagel, T.A. Lograsso, L.L. Miller, Physical properties of Heusler-like Fe_2 VAl, Phys. Rev. B 63 (16) (2001).
[72] T. Gasi, V. Ksenofontov, J. Kiss, S. Chadov, A.K. Nayak, M. Nicklas, J. Winterlik, M. Schwall, P. Klaer, P. Adler, C. Felser, Iron-based Heusler compounds Fe_2 YZ: Comparison with theoretical predictions of the crystal structure and magnetic properties, Phys. Rev. B 87 (6) (2013).
[73] F. Garmroudi, M. Parzer, M. Knopf, A. Riss, H. Michor, A.V. Ruban, T. Mori, E. Bauer, Unveiling the structure-property relationship in metastable Heusler compounds by systematic disorder tuning, Phys. Rev. B 107 (1) (2023) 014108.
[74] S. Wurmehl, M. Wójcik, Structural order in Heusler compounds, in: C. Felser, A. Hirohata (Eds.), Heusler Alloys: Properties, Growth, Applications, Springer International Publishing, Cham, 2016, pp. 87–109.
[75] P. Neibecker, M.E. Gruner, X. Xu, R. Kainuma, W. Petry, R. Pentcheva, M. Leitner, Ordering tendencies and electronic properties in quaternary Heusler derivatives, Phys. Rev. B 96 (16) (2017).
[76] A. Hirohata, J. Sagar, L.R. Fleet, S.S.P. Parkin, Heusler alloy films for spintronic devices, in: C. Felser, A. Hirohata (Eds.), Heusler Alloys: Properties, Growth, Applications, Springer International Publishing, Cham, 2016, pp. 219–248.
[77] R.E. Watson, L.H. Bennett, Transition metals: d-band hybridization, electronegativities and structural stability of intermetallic compounds, Phys. Rev. B 18 (1978) 6439–6449.
[78] R. Nahar, K.M. Law, T. Roden, M. Zengel, J. Lewis, S. Budhathoki, R. Nold, H. Avlani, B. Akintunde, N. Derksen, Dataset on density functional theory investigation of ternary Heusler alloys, Data Brief. 52 (2024) 109971.
[79] P. Giannozzi, O. Andreussi, T. Brumme, O. Bunau, M.B. Nardelli, M. Calandra, R. Car, C. Cavazzoni, D. Ceresoli, M. Cococcioni, N. Colonna, I. Carnimeo, A. D. Corso, S. de Gironcoli, P. Delugas, R.A.D. Jr, A. Ferretti, A. Floris, G. Fratesi, G. Fugallo, R. Gebauer, U. Gerstmann, F. Giustino, T. Gorni, J. Jia, M. Kawamura, H.Y. Ko, A. Kokalj, E. Kucukbenli, M. Lazzeri, M. Marsili, N. Marzari, F. Mauri, N. L. Nguyen, H.V. Nguyen, A.O. de-la Roza, L. Paulatto, S. Ponce, D. Rocca, R. Sabatini, B. Santra, M. Schlipf, A.P. Seitsonen, A. Smogunov, I. Timrov, T. Thonhauser, P. Umari, N. Vast, X. Wu, S. Baroni, Advanced capabilities for materials modelling with Quantum ESPRESSO, J. Phys. Condens Matter 29 (46) (2017) 465901.
[80] P. Giannozzi, S. Baroni, N. Bonini, M. Calandra, R. Car, C. Cavazzoni, D. Ceresoli, G.L. Chiarotti, M. Cococcioni, I. Dabo, A.D. Corso, S. de Gironcoli, S. Fabris, G. Fratesi, R. Gebauer, U. Gerstmann, C. Gougoussis, A. Kokalj, M. Lazzeri, L. Martin-Samos, N. Marzari, F. Mauri, R. Mazzarello, S. Paolini, A. Pasquarello, L. Paulatto, C. Sbraccia, S. Scandolo, G. Sclauzero, A.P. Seitsonen, A. Smogunov, P. Umari, R.M. Wentzcovitch, QUANTUM ESPRESSO: a modular and open-source software project for quantum simulations of materials, J. Phys. Condens Matter 21 (39) (2009) 395502.
[81] J.P. Perdew, K. Burke, M. Ernzerhof, Generalized gradient approximation made simple, Phys. Rev. Lett. 77 (18) (1996) 3865–3868.
[82] A.D. Corso, Pseudopotentials periodic table: from H to Pu, Comput. Mater. Sci. 95 (2014) 337–350.
[83] S. Nepal, R. Dhakal, I. Galanakis, Ab initio study of the half-metallic full-Heusler compounds Co_2 ZAl [Z = Sc, Ti, V, Cr, Mn, Fe]; the role of electronic correlations, Mater. Today Commun. 25 (2020) 101498.
[84] F.D. MurnaghanThe compressibility of media under extreme pressures, Proceedings of the National Academy of Sciences 30(9), 1944. pp. 244-247. .
[85] T. Yang, J. You, L. Hao, R. Khenata, Z.-Y. Wang, X. Wang, Structural configuration and phase stability in full Heusler alloys Cr_2 ZnSi and Cr_2 ZnGe, J. Magn. Magn. Mater. 498 (2020) 166188.
[86] J.J. Jorgensen, G.L.W. Hart, Effectiveness of smearing and tetrahedron methods: best practices in DFT codes, Model. Simul. Mater. Sci. Eng. 29 (6) (2021).
[87] P.E. Blöchl, O. Jepsen, O.K. Andersen, Improved tetrahedron method for Brillouin-zone integrations, Phys. Rev. B 49 (23) (1994) 16223–16233.
[88] K. Momma, F. Izumi, VESTA 3 for three-dimensional visualization of crystal, volumetric and morphology data, J. Appl. Crystallogr. 44 (6) (2011) 1272–1276.
[89] V.G. de Paula, M.S. Reis, All-d-metal full Heusler alloys: a novel class of functional materials, Chem. Mater. 33 (2021) 5483–5495.
[90] J. Finley, L. Liu, Spintronics with compensated ferrimagnets, Appl. Phys. Lett. 116 (11) (2020) 110501.
[91] Y. Shen, D. Kan, Z. Tan, Y. Wakabayashi, Y. Shimakawa, Tuning of ferrimagnetism and perpendicular magnetic anisotropy in $NiCo_2$ O_4 epitaxial films by the cation distribution, Phys. Rev. B 101 (9) (2020) 094412.
[92] Y. Zhang, X. Feng, Z. Zheng, Z. Zhang, K. Lin, X. Sun, G. Wang, J. Wang, J. Wei, P. Vallobra, Y. He, Z. Wang, L. Chen, K. Zhang, Y. Xu, W. Zhao, Ferrimagnets for spintronic devices: from materials to applications, Appl. Phys. Rev. 10 (1) (2023) 011301.
[93] National Center For Biotechnology Information, Atomic radius in the periodic table of elements, PubChem (2024).
[94] A. Hirohata, M. Kikuchi, N. Tezuka, K. Inomata, J. Claydon, Y. Xu, G. van de Laan, Heusler alloy/semiconductor hybrid structures, Curr. Opin. Solid State Mater. Sci. 10 (2) (2006) 97–103.
[95] J.C. Slater, The ferromagnetism of Nickel, Phys. Rev. 49 (7) (1936) 537–545.
[96] L. Pauling, The nature of the interatomic forces in metals, Phys. Rev. 54 (11) (1938) 899–904.
[97] G.H. Fecher, H.C. Kandpal, S. Wurmehl, C. Felser, G. Schönhense, Slater-Pauling rule and Curie temperature of Co_2 -based Heusler compounds, J. Appl. Phys. 99 (8) (2006).
[98] J. Kübler, First principle theory of metallic magnetism, Phys. B+C 127 (1) (1984) 257–263.
[99] K.M. Law, R. Nahar, R. Nold, M. Zengel, J. Lewis, A.J. Hauser, Phase and d-d hybridization control via electron count for material property control in the X_2 FeAl material class, J. Magn. Magn. Mater. 596 (2024) 171932.
[100] K. Sumida, Y. Sakuraba, K. Masuda, T. Kono, M. Kakoki, K. Goto, W. Zhou, K. Miyamoto, Y. Miura, T. Okuda, A. Kimura, Spin-polarized Weyl cones and giant anomalous Nernst effect in ferromagnetic Heusler films, Commun. Mater. 1 (1) (2020) 89.
[101] Y. Kurosaki, S. Yabuuchi, A. Nishide, N. Fukatani, J. Hayakawa, Crystal growth and flat-band effects on thermoelectric properties of Fe_2 TiAl-based full-Heusler thin films, AIP Adv. 10 (11) (2020) 115313.
[102] N. Regnault, Y. Xu, M.-R. Li, D.-S. Ma, M. Jovanovic, A. Yazdani, S.S.P. Parkin, C. Felser, L.M. Schoop, N.P. Ong, R.J. Cava, L. Elcoro, Z.-D. Song, B.A. Bernevig, Catalogue of flat-band stoichiometric materials, Nature 603 (7903) (2022) 824–828.
[103] L. Chen, F. Xie, S. Sur, H. Hu, S. Paschen, J. Cano, Q. Si, Emergent flat band and topological Kondo semimetal driven by orbital-selective correlations, Nat. Commun. 15 (1) (2024) 5242.
[104] S. Kirklin, J.E. Saal, B. Meredig, A. Thompson, J.W. Doak, M. Aykol, S. Rühl, C. Wolverton, The open quantum materials database (OQMD): assessing the accuracy of DFT formation energies, npj Comput. Mater. 1 (1) (2015).
[105] J.E. Saal, S. Kirklin, M. Aykol, B. Meredig, C. Wolverton, Materials design and discovery with high-throughput density functional theory: the open quantum materials database (OQMD), Jom 65 (11) (2013) 1501–1509.
[106] D.P. Rai, R.K. Thapa, Study of electronic, magnetic, optical and elastic properties of Cu_2 MnAl a gapless full Heusler compound, J. Alloy. Compd. 612 (2014) 355–360.
[107] S. Nakagawa, Y. Mitsui, R. Kobayashi, R.Y. Umetsu, K. Takahashi, K. Koyama, Magnetic-field-induced decomposition in Cu_2 MnAl Heusler alloys, J. Magn. Magn. Mater. 540 (2021) 168411.